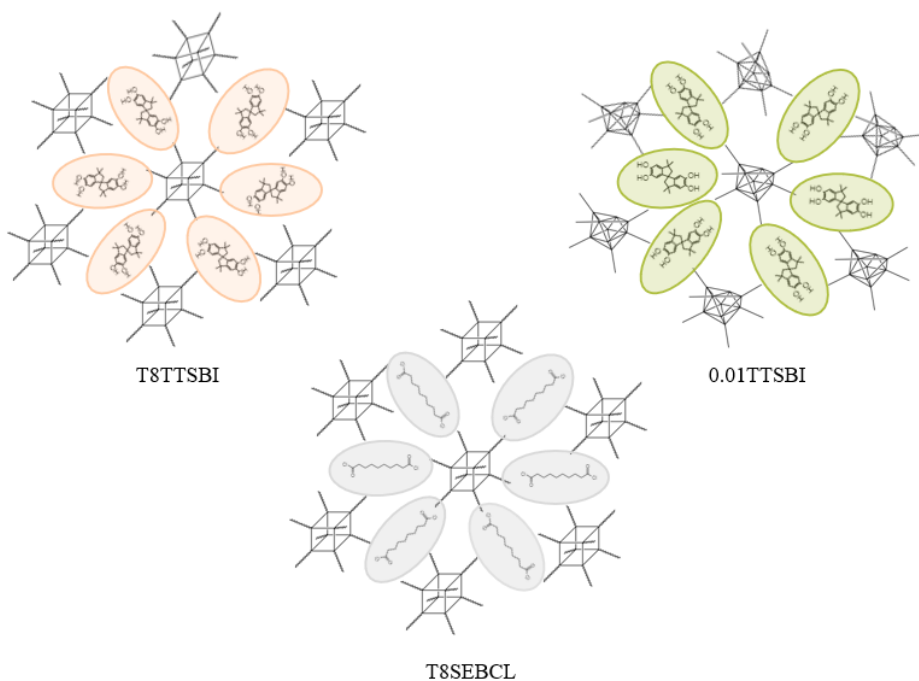




**AALBORG UNIVERSITY**  
DENMARK

# SYNTHESIS AND CHARACTERIZATION OF INORGANIC-ORGANIC HYBRID SILSESQUOXANES-BASED POROUS NETWORKS TOWARDS ADSORPTION PROCESSES



B. BALLARINI



**AALBORG UNIVERSITY**  
DENMARK

**Department of Chemistry and Bioscience**

Fredrik Bajers Vej 7H

DK-9220 Aalborg Ø

<http://en.bio.aau.dk>

**Title:**

Synthesis and characterization of inorganic-organic hybrid silsesquioxanes-based porous networks towards adsorption processes

**Theme:**

Materials Chemistry

**Project Period:**

Fall 2021 - Spring 2022

**Participant(s):**

Barbara Ballarini

**Supervisor(s):**

Donghong Yu

Morten Matstrup Smedskjær

**Page Numbers:** 60

**Date of Completion:**

June 9, 2022

**Abstract:**

The synthesis of silsesquioxanes-based (SQ) porous polymers was constituted by two main steps: the synthesis of the precursors, and the polymerization between the organic and inorganic part. The sol-gel process was used for the synthesis of SQs, while the organic part, 5,5',6,6'-tetrahydroxy - 3,3,3',3'-tetramethyl-1,1'-spirobisindane (TTSBI), was synthesised via cyclization reaction. The follow-on cross-linking reactions were based on Schotten-Baumann reaction and Michael addition. The obtained SQ-cages and hybrids were characterized with  $^{13}\text{C}$  NMR,  $^1\text{H}$  NMR and ATR-FTIR. A total of three hybrids were obtained, respectively called 0.01TTSBI, T8TTSBI and T8SEBCL, which differ in structure and composition. The first is made by a random SQs network covalently bonded with TTSBI, while the last two share the cubic silsesquioxane structure ( $T_8$ ), however T8TTSBI is combined with oxidised TTSBI, while T8SEBCL is combined with sebacoyl chloride. These three hybrids were used as adsorbents in adsorption studies. The results showed that 0.01TTSBI was the most versatile, as it could adsorb in different quantities all the dyes and the heavy metal ion tested. Overall, it is concluded that the main mechanism of adsorption is chemisorption, combined with physisorption for 0.01TTSBI.

*The content of this report is freely available, but publication (with reference) may only be pursued due to agreement with the author.*

# Preface

This work is a Master thesis project carried out at the Department of Chemistry and Bioscience at Aalborg University. The theme is hybrid materials, with focus on organic-inorganic hybrids for dye adsorption studies.

I would like to thank Donghong Yu from the Department for providing guidance in the field of organic chemistry as related to organic synthesis, analysis and laboratory, and Morten Mattrup Smedskjær from the Department for providing guidance in inorganic chemistry and the related property and testing of materials.

Aalborg University, June 9, 2022



---

Barbara Ballarini  
<bballa20@student.aau.dk>

---

<b>Abbreviation</b>	<b>Description</b>
AAS	Atomic absorption spectroscopy
APTES	(3-Aminopropyl)triethoxysilane
ATR	Attenuated total reflectance
BCP	Block copolymer
CV	Crystal violet
EWG	Electron withdrawing group
FT	Fourier transformation
IBX	o-Iodoxybenzoic Acid
IFV	Intrinsic free volume
IUPAC	International Union of Pure and Applied Chemistry
NMR	Nuclear magnetic resonance
MB	Methylene blue
MO	Methyle orange
OMIM	Organic molecules of intrinsic microporosity
[OAS-POSS-NH <sub>3</sub> ]	T <sub>8</sub> with NH <sub>3</sub> functionalities
OVS	Octavinylsilsesquioxane
PIM	Polymers of intrinsic microporosity
POSS	Polyoctahedral oligomeric silsesquioxanes
SQ	Silsesquioxane
T <sub>8</sub>	cubic silsesquioxane cage
TA	Thermal analysis
TFA	Trifluoroacetic acid
TGA	Thermogravimetric analysis
TTSBI	5,5',6,6'-tetrahydroxy-3,3',3',3'-tetramethyl-1,1'-spirobisindane
UV/Vis	Ultraviolet and visible light

# Table of content

<b>Preface</b>	<b>3</b>
<b>1 Introduction</b>	<b>7</b>
<b>2 Problem Analysis</b>	<b>8</b>
2.1 Hybrid materials . . . . .	8
2.2 Polyhedral oligomeric silsesquioxanes . . . . .	9
2.3 Hybrid porous networks . . . . .	11
2.4 Waste water treatment . . . . .	12
2.5 Problem statement . . . . .	13
<b>3 Theory</b>	<b>14</b>
3.1 Sol-gel . . . . .	14
3.1.1 Hydrolysis and condensation . . . . .	15
3.1.2 Water to precursor ratio for porosity control . . . . .	16
3.1.3 Hydrolytic condensation of silsesquioxanes . . . . .	16
3.1.4 Aging and drying of the gel . . . . .	16
3.2 Organic molecules of intrinsic microporosity . . . . .	17
3.3 Network formation . . . . .	18
3.3.1 Michael addition . . . . .	18
3.3.2 Schotten-Baumann reaction . . . . .	19
3.4 Adsorption isotherms . . . . .	20
3.4.1 Adsorption models . . . . .	20
3.4.2 Adsorption kinetics . . . . .	22
<b>4 Methods &amp; Experimental design</b>	<b>23</b>
4.1 Synthesis of cage-like silsesquioxanes . . . . .	23
4.1.1 Experimental considerations . . . . .	23
4.1.2 Procedure with trifluoroacetic acid as a catalyst . . . . .	24
4.1.3 Procedure with Hydrochloric acid as a catalyst . . . . .	24
4.2 Synthesis of TTSBI . . . . .	25
4.2.1 Experimental considerations . . . . .	25
4.2.2 Procedure . . . . .	25
4.3 Cross-linking between sebacoyl chloride and [OAS-POSS-NH <sub>3</sub> ] . . . . .	26
4.3.1 Experimental considerations . . . . .	26
4.3.2 Procedure . . . . .	26
4.4 Cross-linking between TTSBI and random SQs structures . . . . .	27
4.4.1 Experimental considerations . . . . .	27
4.4.2 Procedure . . . . .	27
4.5 Cross-linking between TTSBI and [OAS-POSS-NH <sub>3</sub> ] . . . . .	28

---

4.5.1	Experimental considerations . . . . .	28
4.5.2	Procedure . . . . .	28
4.6	Dye & heavy metal ion adsorption experiments . . . . .	29
4.7	Analysis . . . . .	30
4.7.1	ATR-FTIR . . . . .	30
4.7.2	NMR . . . . .	30
4.7.3	TGA . . . . .	30
4.7.4	UV/Vis & AAS . . . . .	30
<b>5</b>	<b>Results &amp; Discussion</b>	<b>32</b>
5.1	Analysis of SQ structures from HCl catalysis . . . . .	32
5.2	Analysis of SQ structures from TFA catalysis . . . . .	34
5.3	NMR analysis of TTSBI . . . . .	35
5.4	Analysis of hybrids . . . . .	37
5.5	Thermal stability of hybrids . . . . .	39
5.6	Adsorption isotherms . . . . .	40
5.7	Adsorption kinetics . . . . .	45
5.8	Reusability test . . . . .	47
5.9	General discussion . . . . .	47
<b>6</b>	<b>Conclusion</b>	<b>51</b>
<b>7</b>	<b>Perspective</b>	<b>52</b>
	<b>Bibliography</b>	<b>53</b>
	<b>Appendix A Analysis Methods</b>	<b>58</b>
A.1	Attenuated total reflection FT-IR . . . . .	58
A.2	Nuclear magnetic resonance . . . . .	58
A.3	Thermogravimetric analysis . . . . .	59
A.4	Ultra violet and visible spectroscopy . . . . .	59
A.5	Atomic absorption spectroscopy . . . . .	60

# 1 Introduction

Nature is capable of producing functional materials for very specific purposes, adapting the properties of the compounds to the needs of the process, in order to obtain the most efficient result. Therefore, for all living organisms, nature creates a variety of materials, systems and architectures. To combine all the aspects, a high level of sophistication is needed, hence biological materials result from a time dependant process. Furthermore, the scale of biological hierarchical constructions ranges from nanometres, micrometres to millimetres, to accommodate the different processes happening at different levels. [1]

This being said, nature is a teacher for materials science, given that, to meet the requirements of our developing world, new materials should aim at higher levels of miniaturization, be recyclable and reliable. One way to achieve some of these objectives, is to follow nature's ability to combine at nanoscale organic and inorganic components.[2] Some of the earliest examples of hybrids date back to prehistory, with frescoes found in prehistoric caves. Later on, clay-based materials were used by the Romans as bleaching agents, by the Chinese for the shaping and ceramization of porcelain, and as a dye pigment by the Maya. [1] In particular, this dye preserved the intense blue color and withstood the harsh environment until today, thanks to the combined properties of the clay, with its chemical resistance, and to the great organic pigment of colour. [3] Ever since, hybrid materials have been employed, with successful commercial applications reached in 1950s, although the term hybrids was never evoked until the 1980s, when developments in soft inorganic chemistry processes made the synthesis of a number of different hybrids possible.[4]

Materials as flexible as rubber but as strong as steel can be achieved by the combination of nanoscale inorganic composites with high performance polymeric matrices.[5] In recent years, cage-like organosiloxanes have received attention as they can be used as 3D building blocks to construct covalently linked hybrid porous networks, with the possibility to tailor both structure and properties for numerous applications.[6] These materials have a silica cage core with organic substituent attached to each vertex, and are generally categorized as polyoctahedral oligomeric silsesquioxanes (POSS). The cage structure grants a series of advantageous proprieties, such as rigidity, nanoscale, high functionality and thermal stability. Furthermore, these compounds are usually nonvolatile, light weight, odorless and environmentally friendly. [7] Therefore, the possibility for these cage compounds to react with multiple substrates generates porous polymers with high variability in synthetic approaches and applications in gas storage, catalysis, water treatment, *etc.* [6] In this work the focus will be on the synthesis of hybrid POSS porous networks and their applicability for adsorption processes.

# 2 Problem Analysis

## 2.1 Hybrid materials

Following the definition from the International Union of Pure and Applied Chemistry (IUPAC), a hybrid material is that composed of an intimate mixture of organic components, inorganic components or a mixture of two components, which usually interpenetrate on the scales of less than  $1 \mu m$ . [8] In this report the focus will be on organic-inorganic hybrid materials, which are often composites at the molecular or at the nanoscale level. The interest for these compounds emerged not only for the enhanced physical and chemical properties, but also by the numerous possibilities obtained by combing the colloidal state with the chemical properties of biological systems. As such, hybrid materials can be processed as thin films or thick coating, as powders or monoliths, with complex architectures.[1]. The captivating properties of the hybrid materials do not only derive from the individual characteristics of the organic and inorganic part, but also form the the composite's phase morphology and interfacial properties. [9] Therefore, based on the type of interactions present at the interface, these materials are generally divided in two classes which are:

- Class I: hybrids systems in which the organic and inorganic components interact via weak bonds, such as van der Waals forces, hydrogen bonds, or electrostatic bonds
- Class II: hybrid systems in which the organic and inorganic components are linked together by covalent or iono-covalent chemical bonds

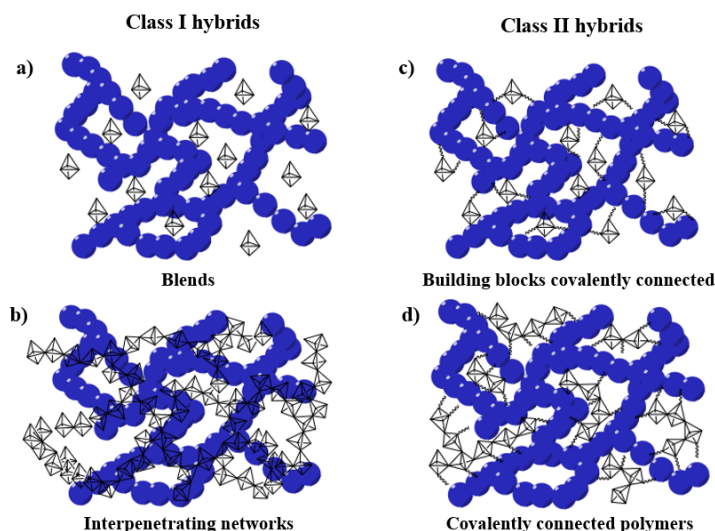


**Figure 2.1.** Schematic representation of class I in a), b) and class II hybrids in c), d), where the blue circles are building block A and the polyhedra are building block B

Naturally, hybrid materials from class II, shown in Figure 2.1, may also posses interaction of hybrids from class I. Class II hybrids are of great interest because of their covalent interactions. The precursors used for this type of hybrids posses at least two type of functionalities, which generally are alkoxy groups and metal to carbon links. The first

generates oxo-polymer frameworks through hydrolysis and condensation reaction, whereas the latter grants the link between the organic and inorganic parts, therefore it has to be stable under hydrolysis conditions. [10] Two principal methods have been developed for the synthesis of these compounds: sequential synthesis and one-step synthesis. In the former, the inorganic network is formed by polycondensation of the alkoxide groups, leading to the formation of oxo-polymer surrounded by organic groups, then the second reaction takes place, in which the organic groups get to polymerise, forming a network. The latter method consists in one step reactions where alkoxy silanes are either grafted on other polymers, or form a network based on Si-C-Si bonds. Regardless of the method, the synthesis involves a sol-gel process, given that the organic part of the hybrid cannot reach high temperatures. [10] Among the great variety of compounds present in the II class, a remarkable place has been taken by polyhedral oligomeric silsesquioxanes. [11]

## 2.2 Polyhedral oligomeric silsesquioxanes

Siloxanes are a group of building blocks for organic-inorganic hybrids, and the simplest one is the silicate group  $SiO_{4/2}$ . Three of the oxygen present can be substituted with an organic group (R), giving  $RSiO_{3/2}$ ,  $R_2SiO_{2/2}$  and  $R_3SiO_{1/2}$  units. Silsesquioxanes are a class of siloxanes, and are constructed from the  $RSiO_{3/2}$  unit alone. [12] The term "silsesquioxane" indicates the presence of silicon (sil-) with one and a half (-sesqui-) bonds with oxygen (-oxane), given the 1.5 ratio between Si and O. [13] A simplified nomenclature for SQs consists in naming the type of silicon unit with a numerical subscript to indicate the number of units in the framework. Thus, depending on how many bonds the Si atom has with oxygen, there can be M, D, T and Q types, which respectively indicate one, two, three and four bonds. Therefore a cubic cage can be addressed as  $T_8$ , shown in Figure 2.2 (d). [14] Eventually, a subscript can be added to denote the type of functional group present of the silicon units. Furthermore, SQs can exist in a multitude of structures such as random, ladder- or cage-type structures, which can be open and closed, and can vary in number of repetitive units between 8, 10 and 12, [15] as shown in Figure 2.2.

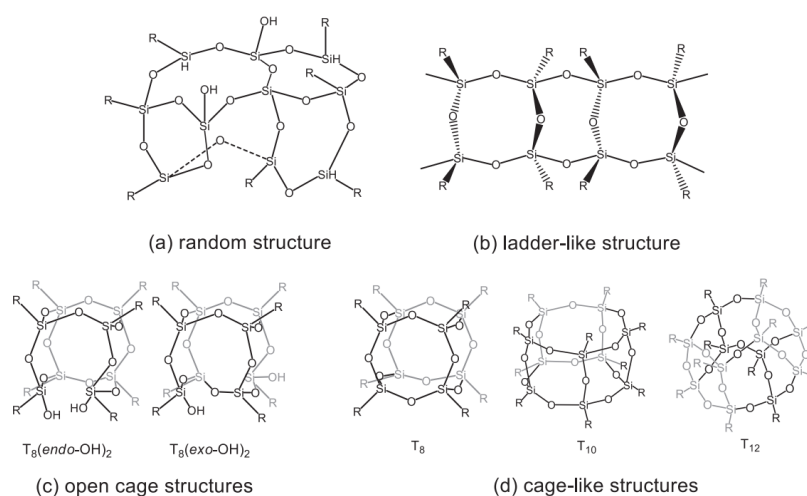


**Figure 2.2.** Representation of (a) random structure, (b) ladder-like structure, (c) open cage structure (endo-OH) and closed cage structure (exo-OH), and (d) cage-like structures with 8, 10, and 12 T units. Figure reprinted from Reference [11]

The most common approach to generate cage-like organosilsesquioxanes is by hydrolytic polycondensation of trichloro- or trialkoxysilanes. [6] From the experimental point of view,  $T_8$ -type structures are the most used because of their solubility in many organic solvents, allowing simple purification and further post-functionalization.  $T_{10}$  and  $T_{12}$  cages are generated from spontaneous rearrangement of the  $T_8$ -type, therefore being a challenge in the synthesis process. The choice of catalyst can help to avoid such formations. However, there is only little information regarding this phenomenon, given that the higher geometry species have been hard to isolate, therefore being regarded as oligomers rather than discrete molecular species. [11]

As mentioned in Section 1, POSS has an inorganic silicate core and an organic covalently bonded outer sphere, generating nanostructures with diameters ranging from 1 to 3 nm, hence being considered as the smallest silica particles. [16] Because of their nanometre scale, SQs with non reactive R groups are able to disperse uniformly within the matrix, thus avoiding phase separation and acting as a network modifying agent, or nanofiller. On the other hand, when reactive groups are present, they will act as a network formers, or cross linkers, reacting with themselves or other components. [15, 17] Furthermore, when choosing the R group, organic substitutes are easily synthesized, given the stable nature of the bond  $Si-C_{sp^3}$ . [17] This gives a large number of hybrid network options for various applications.

Typically, the precursor of choice is a vinyltrimethoxysilane, which gives a cage where the R substituent becomes a vinyl group, called octavinylsilsesquioxane (OVS). This allows a series of post functionalisation reactions such as amination, nitration, click reactions, protonation and coordination, generating a porous polymer. [18] In this report the focus will be on a different precursor, (3-aminopropyl)-triethoxysilane (APTES), which gives a soluble product, and generally allows for more bland reaction condition, given that the resulting product is a salt. [19] The two precursors and the resulting moieties can be seen in Figure 2.3

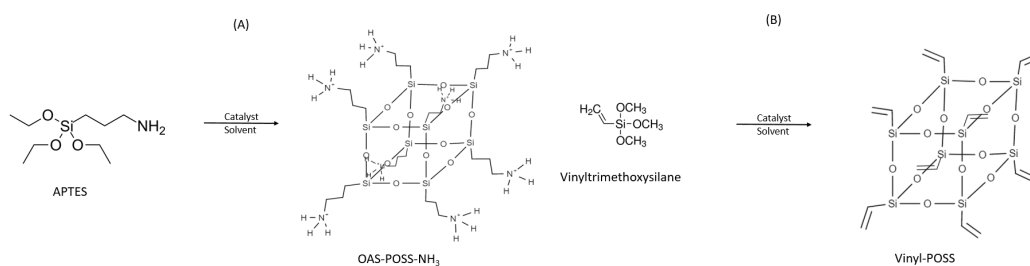


**Figure 2.3.** (A) Cubic compound OAS-POSS-NH<sub>3</sub> yielded from (3-aminopropyl)-triethoxysilane, (B) Cubic compound Vinyl-POSS from vinyltrimethoxysilane.

Different types of catalyst and concentrations between the solvent and APTES will result in different yield and reaction times, as well as different final properties of the product. When the product yielded is homosubstituted amido-functionalized polyoctahedral oligomeric silsesquioxanes, like the one showed in figure 2.3 (A), it can be called OAS-POSS-NH<sub>3</sub> [19, 20]

## 2.3 Hybrid porous networks

Namely, porous materials are materials containing many pores, with a continuously solid phase and a fluid phase constituting the pores, which can be a gas or a liquid. The amount, dimension and type of pores are designed to achieve the desired material's performance. [21] Porous materials can be classified based on the pore size ( $d$ ) as macroporous, mesoporous and microporous with, respectively,  $d > 50\text{nm}$ ,  $2\text{-}50\text{nm}$ , and  $d < 2\text{nm}$ . [22]

Polymeric materials can be tailored to have high surface area and well defined pores structure, as they have quite easy processability; for instance, some can be dissolved in solvents and processed using solvent-based techniques without destroying the porosity. [23, 24] Additionally, porous polymers can incorporate multiple chemical functionalities either in the porous network, or at the pore surface, giving the prospect to produce a wide range of products. Another important characteristic is the self-assembly behaviour, which is conspicuous in biological system with sophisticated architecture and different levels of organization. In polymers this behaviour is observed especially in block copolymers (BCPs), which have been used to prepare meso-/macroporous polymer with well-defined ordered mesopore structures. BCPs used for their self-assembly behaviour are usually hybrid macromolecules, obtained by covalently bonding two or more immiscible homopolymers. Due to their covalent bonds, the phase separation is restricted to the nanometer scale, thus porous polymer can be prepared with the BCP self-assembly methodology. [25] Silicate materials can also be tailored to achieve desired pore size with different synthetic approaches. As such, they can be incorporated in polymer matrices to generate tailored hybrids with enhanced properties. [22] POSS can be incorporated in polymers with four main approaches (Figure 2.4):

1. as a blender or nanofiller, when R groups are non reactive
2. as tethering macromolecule to graft POSS cages onto a polymer backbone, when the POSS cage is mono-functionalised, generating polymers with pendant POSS cages
3. as micro-initiator to initiate polymerization from the surface of the POSS, when the POSS cage is multi-functionalised, generating star-like macromolecules
4. as micro-initiator to produce heavily cross-linked polymer network, when the POSS cage is multi-functionalised and reacts with multi-reactive groups

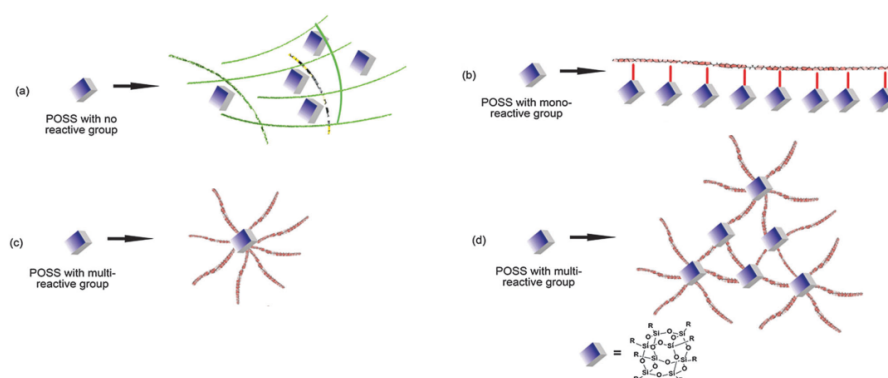


**Figure 2.4.** Schematic representation of POSS as a nanofiller (a), as a tethering molecule (b), as a micro-initiator for star-like macromolecules (c) and as micro-initiator for cross-linked polymer network (d). Figure adapted from Reference [26]

Naturally the incorporation of POSS will change, on the microscopic scale, the polymer matrix topology, as well as the local molecular interactions and the segment mobility. This will result in modulus, strength, glass transition temperature ( $T_g$ ), thermal stability, and dimensional stability alterations on the macroscopic scale. [26] An example of hybrid polymer-POSS is polyamide-POSS material. Polyamides can be found both in natural materials, such as wool and proteins, and in artificial materials such as nylon and aramids, due to their high durability and strength, based on their intermolecular hydrogen bonding. This class of polymer contains amide linkages along their macromolecular contour. A notable example of hybrid polyamide-POSS was prepared by Gnanasekaran et al. as a cost-effective and environmentally friendly biocomposites membranes with no cracks or voids, suitable for purposes like gas transport studies. The enhanced properties were ascribed to increased  $T_g$ , surface roughness and density, and the decreased fractional free volume and surface free energy of the membranes upon increasing the POSS content. [26, 27]

## 2.4 Waste water treatment

Clean and potable water has always been a priority for all kinds of human activities, ranging from domestic uses to industrial and agricultural productions. However, with the increase of said activities came also an increase in the treatment of waste waters containing a number of pollutants harmful to human and animal life. In waste waters, pollutants can be inorganic and organic chemicals, as well as biological agents, heat and radioactive species, therefore, pollutants can be described as substances that change the natural quality of the water. [28] Over the years, this has become a major environmental concern and challenge, giving raise to a variety of technologies and treatments to clean waste waters. In particular, the growing need for synthetic dyes has become problematic, as most of them have teratogenic, carcinogenic, and mutagenic effects or high biological toxicity, producing a serious threat to environment and human health. This can also be said for heavy metal ions, such as nickel, which can be treated with the same techniques used for dye adsorption. [29] The methods commonly used today to remove synthetic dyes can be broadly classified in 3 categories:

- Biological: a combination of aerobic and anaerobic processes generally carried out via enzymatic degradation of pollutants
- Chemical: processes like advanced oxidation process, electrochemical destruction, photochemical and ultraviolet irradiation are some of the main examples
- Physical: conventional methods are adsorption, coagulation, ion exchange and membrane filtration, achieved by the mass transfer mechanism

[30] Generally, all the methods can provide a successful dye removal, however, biological and chemical methods present many drawbacks, such as high operational and maintenance costs, generation of toxic sludge and complicated procedure involved in the treatment. Thus physical methods being the preferred way to remove dyes from waste waters, as these methods are cost efficient, easy to apply and commonly don't produce hazardous by-products. [31] Among the physical methods, adsorption gained attention due to its versatility and wide applicability. The term "adsorption" was first introduced by Kayser in 1881 and refers to a non-reactive process whereby a solid surface is concentrated by a substance initially present in a gaseous or liquid surrounding. This term was introduced

to differentiate between the accumulation of material on the surface and intermolecular penetration, called absorption, shown in Figure 2.5. [28]

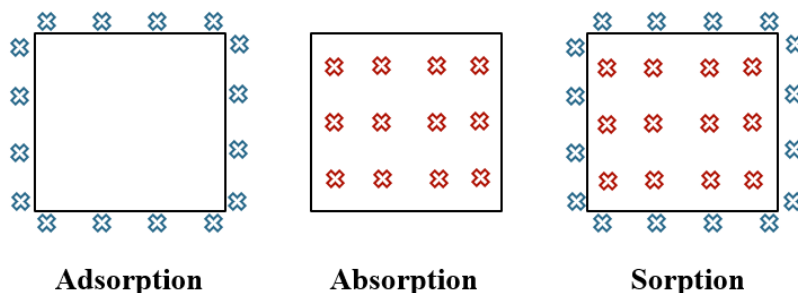


**Figure 2.5.** Schematic representation for the processes of adsorption, absorption and sorption.

Moreover, when adsorption is caused by van der Waals intermolecular forces, it is referred to as physical adsorption or physisorption, whereas it is called chemical adsorption, or chemisorption, if adsorbate and the adsorbent are chemically bonded. [32] When the molecules of the adsorbate are present both on the surface, and in the bulk of the adsorbent, the term sorption is used. The relation between the amount adsorbed and the equilibrium concentration of the adsorbate, at constant temperature, is known as adsorption isotherm. [32]

Accordingly, a good adsorbent should possess a porous structure resulting in a high surface area, and fast adsorption kinetics, given that the adsorption equilibrium should be quickly achieved, in order to remove the pollutant as fast as possible. In addition, the adsorbent should be reusable and, therefore, thermally stable.[28]

## 2.5 Problem statement

The aim of this project is to create a hybrid porous inorganic-organic network with silica-core and organic frame interpenetrated, in order to produce a material that has a rigid porous framework with suitable porosity for dye and heavy metal ion adsorption in waste water treatment. Based on previous studies [6, 29, 33, 34],  $T_8$  SQs and organic molecules of intrinsic microporosity (OMIMs) have shown good results towards adsorption processes, thus the focus will be on achieving a hybrid between these two classes of compounds. OMIMs will be described in Section 3.2.

Therefore the problem statement for this work is:

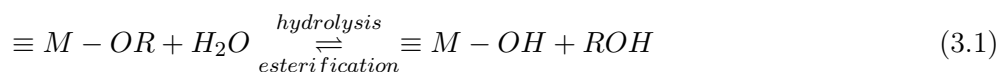
*is it possible to achieve a thermally stable porous inorganic-organic hybrid network with a rigid framework, composed of silsesquioxanes and OMIMs, suitable for adsorption processes?*

# 3 Theory

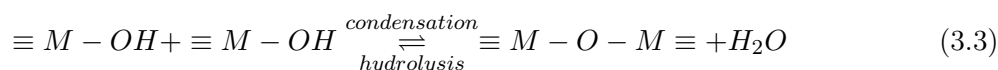
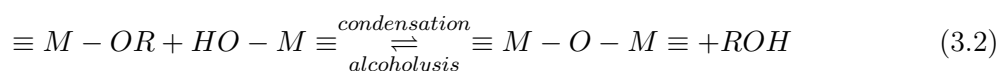
## 3.1 Sol-gel

Hybrid nanocomposites can be achieved with a number of synthetic approaches, but their inorganic portion commonly involves hydrolysis and condensation. Furthermore, this type of materials require moderate temperature, to avoid decomposing the organic part, therefore sol-gel is the preferred method of synthesis, and the final product will depend on the phase separation during the process.[15] The aim of sol-gel processing is to control the surfaces and interfaces of materials during the formation of polymers from solution, through a transformation from liquid precursors to a sol and finally to a network structure called a 'gel'. [35] The sol is a colloidal suspension of solid particles in a liquid in which the "molecules or polymolecular particles dispersed in a medium have at least in one direction a dimension roughly between 1 nm and 1  $\mu\text{m}$ ", following IUPAC definition. This system forms through series of hydrolysis and condensation of the precursor. [36] The most common precursors used are multifunctional alkoxides, given the wide range of alkyl substituent available to control the oxide synthesis, according to the desired reactivity. The steps of the process can be summarised as follows:

1. Formation of the sol from hydrolysis as in equation 3.1, where M is a metal atom and R is an alkyl group



2. Formation of the gel via polycondensation to form metal-oxo-metal or metal-hydroxy-metal bonds, which can give as by product water, as in equation 3.3, or alcohol, as in equation 3.2



3. Aging of the gel, where solvent expulsion and shrinkage happen, while condensation continues within the gel network
4. Drying of the gel either to form a dense 'xerogel' or an aerogel

Eventually, an additional step can be preformed to remove surface M-OH groups, by calcinating the gel at 800°C. [35] The solvent is generally a water with alcohol as homogenising agent, because of the insolubility of alkoxy silanes in water. However, gels can be prepared even without alcohol addition, because of the production of alcohol as a by-product in the hydrolysis reaction, as shown in Equation 3.2. [36]

Hydrolysis and condensation steps are heavily influenced by various factors, such as R-group, solvent, presence and concentration of catalyst, and electronegativity of the metal atom (M).

### 3.1.1 Hydrolysis and condensation

When Silicon is the central atom of the alkoxide precursor, acidic or alkaline catalysis is needed, as the reaction is very slow under neutral conditions. The type of catalysis heavily influences the hydrolysis process, since this step includes a pentacoordinate transition state, therefore the rate relies on the stability of the transition state, which in turn, depends on the electron withdrawing or donating power of the -R or the -OH groups. [35] Hence, successive hydrolysis step will be slowed by acidic catalysis and speed up by alkaline catalysis, as shown in Figure 3.1.

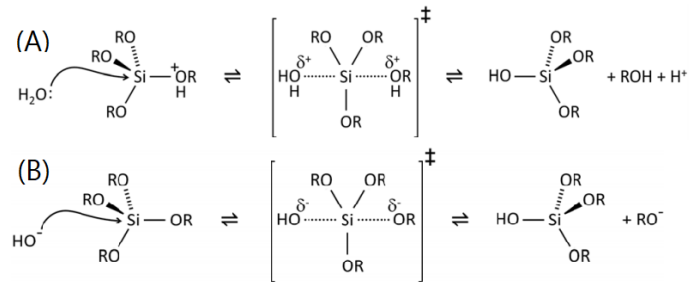


**Figure 3.1.** Reaction scheme for acid catalysed hydrolysis (A), and for base catalysed hydrolysis (B). Figure adapted from Reference [35].

This happens because hydrolysis proceeds via successive nucleophilic attack, hence the nucleophilicity of the incoming group, the  $\delta+$  charge on the Si, and the stability of the leaving group being influenced by the type of catalysis. The mechanism is hypothesized as a nucleophilic substitution ( $S_N2$ ), thus the reaction rate depending on steric hindrance of the Silicon atom, and the complexity of the alkyl chain on the alkoxide. [37]

Similarly, condensation can be catalysed by acidic or alkaline conditions, as in Figure 3.2, and the rate will depend on the amount of the precursor that has been already hydrolysed. Accordingly, for an acid catalysed hydrolysis, the condensation process will begin before the hydrolysis is complete, resulting in network-like gels, whereas for basic conditions multiple condensation steps can happen simultaneously, generating highly branched agglomerates in the sol, which crosslink forming a colloidal gel. [35]

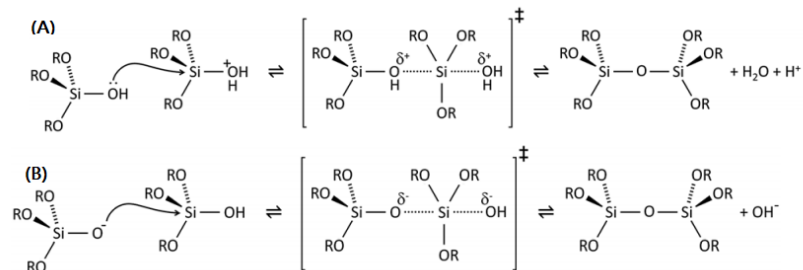


**Figure 3.2.** Reaction scheme for acid catalysed condensation (A), and for base catalysed condensation (B). Figure adapted from Reference [35].

Acid catalysis is preferred commonly when working with Silicon precursors, because the

basic conditions could cause decomposition of the polyoctasilsesquioxane core. [19]

### 3.1.2 Water to precursor ratio for porosity control

Water is a key parameter to control the sol to gel transition and the gelation time. This becomes clear from the stoichiometry of the reaction in Equation 3.4, where if  $n=4$ , the reaction goes to completion, using 4 molecules of water to generate 4 molecules of alcohol, hence resulting in a full hydrolysis of a tetravalent Silicon precursor. [35, 37]



From experimental works [38, 39] it was possible to comprehend that higher ratios of water result in longer gelation times, and promotes the formation of higher ratio of bridging to non-bridging oxygen, thus generating a more polymerised and branched structure. Additionally,  $N_2$  adsorption-desorption isotherms show that alkoxy silane precursors yield microporous materials, identified by a type I isotherm, reaching saturation at low  $P/P_0$  values, without hysteresis loop. Specific investigation on  $H_2O/Si$  ratio showed that the volume adsorbed increases with increasing  $H_2O/Si$  ratio, while presenting also a smoothing on the isotherm knee, which indicates the presence of a wide range of pores diameters. [37] Moreover, the presence of water influences textural properties such as surface area and pore volume, giving an increase of respectively  $\approx 300 \text{ m}^2/\text{g}$  and  $\approx 200 \text{ cm}^3/\text{g}$  when the amount of water is increased. [37]

### 3.1.3 Hydrolytic condensation of silsesquioxanes

The sol-gel reactions involving silsesquioxane are usually time consuming and complex multi-step processes, [13] although they can be simply summarised by the following reaction scheme 3.5



The complexity is given by the multiple influencing factors over this reaction, such as the concentration of  $RSiX_3$ , solvent, nature of R and X groups, catalyst, water addition and solubility of condensation products. As mentioned before, multiple structures can be obtained as final product, and this happens because during the reaction multiple intermediate form, hence by controlling the reaction conditions it is possible to favor the equilibrium towards a the formation of specific structures. Therefore, there is no universal procedure, however general trends can be observed. The formation of silsesquioxane polymers is promoted by high concentration of Si precursor, polar solvent, high pH, more reactive X and R groups and higher additions of water. Vice versa, intramolecular cyclization reactions that yield cage structures are promoted by dilute reaction solution of  $RSiX_3$ , non-polar solvents, low pH and adequate amounts of water. Finally, the less soluble SQs species that precipitate during reaction, draw the equilibrium of the reaction species towards forming more of the less soluble product. [13]

### 3.1.4 Aging and drying of the gel

Once the gel is formed from the hydrolysis and polycondensation reaction, the product is subject to drying and heat treatment to obtain the final product. During this process

water and solvent molecules physically bound to the gel are desorbed by increasing the temperature of the gel to 100°C. This leads to formation of "cracks" and deformation of the original porous backbone, given by the capillary pressure created by the evaporation of the solvent and the low permeability of the gel. Hence the difference in the contraction speed between the outside and the inside of the gel generating a xerogel, a dense material with disordered porosity. The cracking can be countered by aging the gel prior to the drying process. The aging consists in leaving the wet gel to react for longer, thus allowing the formation of new crosslinks, which leads to shrinkage of the wet gel and increases the modulus and viscosity of the gel, reducing the successive drying shrinkage and hence reducing crack formation. When the pore liquid in the gel is substituted by air with moderate shrinkage of the matrix, aerogels are obtained. [37]

### 3.2 Organic molecules of intrinsic microporosity

When organic molecules form solids, they pack space efficiently in order to minimize the amount of void space. Generally, this leads the molecules to form a crystal structure, but when molecules have a complex shape the crystallization process happens slowly, leading to the formation of an amorphous glass material. The glass state impedes translational molecular movements, thus the molecules are kinetically trapped and unable to rearrange into more thermodynamically stable crystals. This packing produces low density that is able to generate microporous materials. This happens especially when the molecule is designed with a shape that is "awkward" to pack in space, trapping enough free volume so that the final solid will act as a microporous material, with interconnected pores of less than 2nm diameter. This class of molecules is called organic molecules of intrinsic microporosity. [34] An example is triptycene, the smallest molecule in an iptycene family, which is a class of aromatic compounds. This molecule generated interest due to the unusual internal free volume (IFV), which was first introduced by Swager et al. as "the volume defined by the rigid aromatic faces of the triptycene", shown in Figure 3.3.

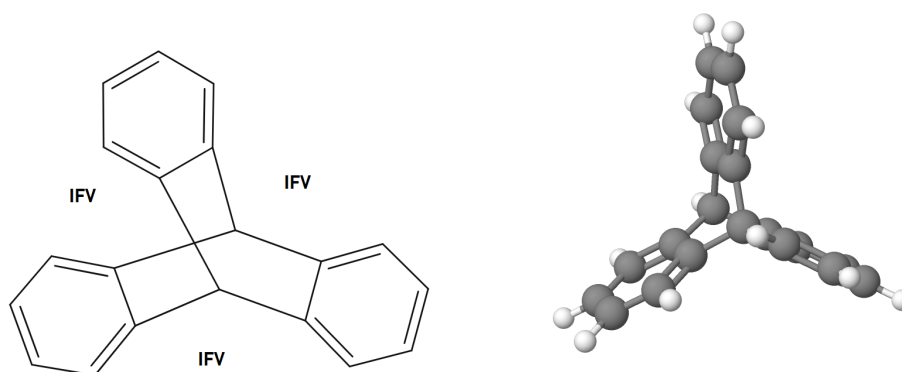


**Figure 3.3.** 2D and 3D representation of the triptycene molecule, with indication of the intrinsic free volume placing. In the 3D figure, the gray represent carbon and the white represents hydrogen

In a general sense, the concept of OMIMs involves the design of rigid discrete molecules,

made by structural components with well-defined geometries, that give inefficient space packing, thus providing sufficient free volume for microporosity, which can be demonstrated by gas adsorption.[34] Mathematical packing problems have been linked to the behaviour of real particles and molecules by developing the concept of "random jamming", that can be directly correlated to the glass transition temperature ( $T_g$ ) of a molecular material, at which concerted molecular motions cease. [34] Using the idealized hard-sphere model, in which the behaviour of a liquid is studied by ideally assuming that the liquid is composed of hard spheres, the relation between the temperature ( $T$ ) and the packing in and euclidean space is described by the following Equation 3.6

$$\frac{p}{\rho k_B T} = 1 + 2^{d-1} \phi g_2(D^+) \quad (3.6)$$

where  $p$  is the pressure,  $\phi$  is the packing fraction,  $\phi g_2(D^+)$  the contact value of the pair correlation function and  $d$  is the distance between spheres. Therefore, the rapid compression of a hard-sphere liquid, under the constraint that significant crystal nucleation is suppressed, can produce a range of metastable branches. The density end points of the branches are disordered "jammed" packings, which can be regarded to be glasses. Moreover, a slow compression leads to a higher random jammed density than a fast compression. [40]

When OMIMs are polymerised, they can generate network polymers of intrinsic microporosity (PIMs), in which the porosity is given by the inefficient amorphous packing of the rigid and contorted macromolecular chains, despite the lack of a network structure.[41] For the purpose of this project, a suitable OMIM, describe in Section 4.2, will be synthesised to fit in an hybrid polymer with  $T_8$  SQ.

### 3.3 Network formation

The hybrid designed for dye adsorption is a combination between the monomers 5,5',6,6'-tetrahydroxy - 3,3,3',3'-tetramethyl-1,1'-spirobisindane and [OAS-POSS-NH<sub>3</sub>], as the desired characteristics are high surface area and thermal stability. However, the formation of two more hybrids is also investigated, as it can be of interest to see how the final characteristics of hybrids with a more flexible design compare to a more rigid hybrid. Therefore, two additional copolymers, between sebacoyl chloride and [OAS-POSS-NH<sub>3</sub>], and between TTSBI and SQs random structures, are synthesized. The polymerisation between the organic and inorganic part of the hybrid is dependent on the type of bond that will be formed, thus, different types of reactions are employed to achieve the desired bond, which will be described in this section. The reaction between TTSBI and SQs random structures will be carried out as a sol-gel condensation, described already in Section 3.1.

#### 3.3.1 Michael addition

For the reaction between  $T_8$  and TTSBI will involve the formation of an amine, therefore the reaction employed will be an aza-Michael addition. Michael's addition is of great importance because it allows the formation of C-C covalent bonds in mild conditions, therefore extending the carbon chain. This reaction usually refers to the formation of a carbon bond between and  $\alpha, \beta$ -unsaturated carboxylic acid derivative and an enolate as the nucleophile. The best results are achieved when the enolate presents two electron

withdrawing groups (EWG), as these enolates are relatively weak bases, giving addition at the  $\beta$ -carbon of many  $\alpha, \beta$ -unsaturated carboxylic acid derivative, because of the scarce reactivity of carbonyl group in  $\alpha, \beta$ -unsaturated aldehydes, amides, ketones and esters.[42] Therefore the product formed in most cases is a 1,5-dicarbonyl compound.

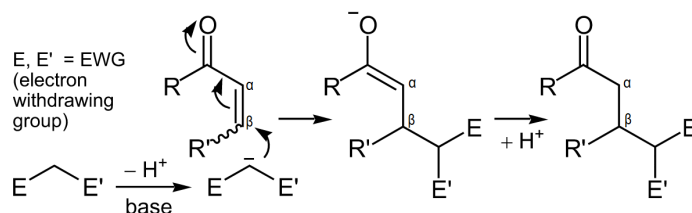


**Figure 3.4.** Reaction mechanism of Michael addition on a  $\alpha, \beta$ -unsaturated carboxylic acid derivative.

The mechanism, showed in Figure 3.4, starts with a base removing a proton from the  $\alpha$ -carbon of the carbon acid, then the enolate adds to the  $\beta$ -carbon of the  $\alpha, \beta$ -unsaturated compound, and the  $\alpha$ -carbon obtains a proton from the solvent. Other reactions have been derived from this mechanism, in particular aza-Michael reactions involve a primary or secondary amine, as the Michael donor, and an activated double bond, as the Michael acceptor. This reaction can also be conducted at room temperature, and generally has a high atom economy. [43]

### 3.3.2 Schotten-Baumann reaction

The reaction between sebacoyl chloride and  $T_8$  will result in the formation of an amide bond, therefore Schotten-Baumann procedure will be used. This procedure was devised to achieve a controlled and reproducible process for formations of amides, which are of primary importance for a variety of industrially relevant polymeric materials. This procedure, for which a general scheme is shown in Figure 3.5, consists in a biphasic reaction between acid chlorides and amines under alkaline conditions. The base usually stays in the water phase, neutralizing the acid generated in the reaction, while the monomers and the products stay in the organic phase.

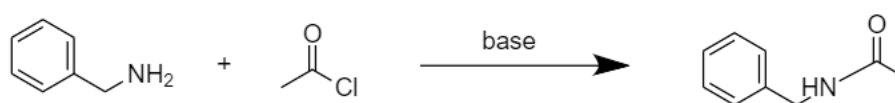


**Figure 3.5.** Schematic representation of the Schotten-Baumann reaction between benzylamine and acetyl chloride, which generates an amide.

The base is usually in excess, to ensure that the pH stays high enough. This process is also carried with a high degree of agitation, because of possible mass-transfer limitations, and the side products are caused by the hydrolysis of the acid chloride. [44]

### 3.4 Adsorption isotherms

The process of adsorption was mentioned in Section 2.4, and it can be described as a mass transfer process which involves the accumulation of substances at the interface of two phases, such as, liquid–liquid, gas–liquid, gas–solid or liquid–solid interface. In water treatment it is preferable that the interactions between adsorbent and adsorbate are weak, thus physisorption being the preferred process, as weak interactions are reversible and can form multi layers of adsorbate. Given that physical adsorption generates a decrease in free energy and entropy, this process is generally exothermic. When the adsorption happens in a solid-liquid system, the adsorbate accumulates at the surface of the solid adsorbent, while the remaining solute reaches a dynamic equilibrium with that adsorbed on the solid phase. The amount of adsorbate that can be taken up by an adsorbent, as function of temperature and concentration of adsorbate, can be described by the adsorption capacity Equation 3.7

$$Q_e = \frac{(C_0 - C_e)V}{m} \quad (3.7)$$

Where  $Q_e$  (mg/g) is the amount of adsorbate per mass unit of adsorbent at equilibrium,  $C_0$  (mg/L) and  $C_e$  (mg/L) are the initial and equilibrium concentration of adsorbate,  $V$  (L) is the volume of the solution, and  $m$  (g) is the mass of adsorbent. [31] The plot of  $Q_e$  versus  $C_e$  at constant temperature is known as adsorption isotherm. [32] The isotherms can be fitted using different models to extrapolate more information about the adsorbent.

#### 3.4.1 Adsorption models

An isotherm model is Langmuir model. Firstly, this model assumes that the solid surface is uniform, that only a monolayer can be formed, that adsorbed molecules don't interact with each other, and are localized in specific sites. The linear form can be written as in Equation 3.8, whereas the non-linear form, displayed in Figure 3.6, is shown in Equation 3.9

$$\frac{C_e}{Q_e} = \frac{1}{Q_m K_L} + \frac{1}{Q_m} C_e \quad (3.8) \quad Q_e = \frac{Q_m K_L C_e}{1 + K_L C_e} \quad (3.9)$$

Where  $Q_m$  (mg/g) and  $K_L$  (L/mg) are Langmuir constants related to maximum adsorption capacity and constant related to the free energy of adsorption, which can be correlated with the variation of the suitable area and porosity of the adsorbent. Thus a higher adsorption capacity will indicate a greater pore volume and surface area. These parameters can be computed from the slope and intercept of the linear plot of  $C_e/Q_e$  versus  $C_e$ . Moreover, Langmuir model can estimate the affinity between the adsorbent and the adsorbate via dimensionless separation factor,  $R_L$ , determined using the following Equation 3.10

$$R_L = \frac{1}{1 + K_L C_0} \quad (3.10)$$

Therefore, when  $R_L=1$  the adsorption is linear, when  $R_L>1$  the adsorption is unfavorable, when  $R_L=0$  it is irreversible and when  $0<R_L<1$  it is favorable. However in most cases the interactions between adjacent adsorbed molecules cannot be ignored. Hence a similar model, that derives from Langmuir assumptions, is the Jovanovic model, with the addition of the possibility of some mechanical contacts between the adsorbing and desorbing molecules. The linear form for this model can be see in Equation 3.11, and the non-linear form is displayed in Equation 3.12

$$\ln Q_e = \ln Q_{max} - K_J C_e \quad (3.11) \quad Q_e = Q_{max}(1 - e^{-K_J C_e}) \quad (3.12)$$

where  $Q_e$ (mg/g) is the amount of adsorbate in the adsorbent at equilibrium,  $Q_{max}$  is maximum uptake of adsorbate obtained from the plot of  $\ln Q_e$  versus  $C_e$ , and  $K_J$  Jovanovic constant. [45]

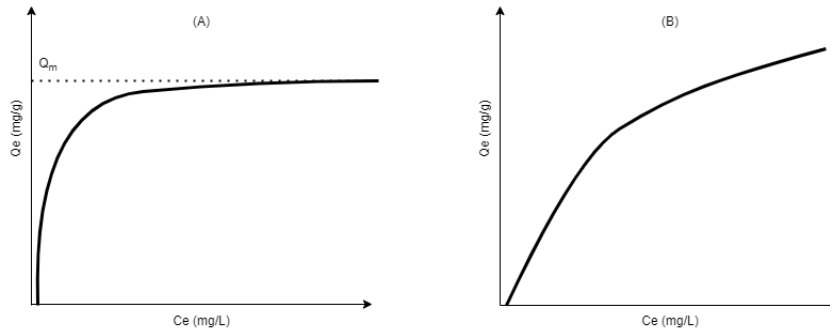


**Figure 3.6.** Schematic representation of Langmuir (A) and Freundlich (B) adsorption isotherms, with the adsorption capacity per gram of adsorbent ( $mg/g$ ) versus equilibrium concentration ( $mg/L$ ) at fixed T.

An alternative, is the empirical Freundlich isotherm model, which is employed to describe the adsorption on an heterogeneous surface with the interaction between adsorbed molecules in the reversible and non-ideal adsorption process. The linear and the non-linear form of this model are expressed, respectively, in Equation 3.13 and 3.14

$$\ln Q_e = \ln K_F + \frac{1}{n_F} \ln C_e \quad (3.13) \quad Q_e = K_F C_e^{1/n_F} \quad (3.14)$$

Where  $K_F$ (mg/g) is a constant indicative of the relative adsorption capacity of the adsorbent, and  $n_F$  is the heterogeneity factor, which accounts for the favourability of the adsorption process. When plotting  $\ln C_e$  against  $Q_e$ , the values for  $n_F$  and  $K_F$  can be obtained from slope and the intercept, respectively. [46] The models just described are two parameters model, however also three parameter model can be used, and the most commonly used is the Sips model. The Sips isotherm follows a combination of Freundlich and Langmuir models, and is suitable to predict the adsorption on heterogeneous surfaces, as it combines the approach of an homogeneous and heterogeneous model, while avoiding the usual limitation for low concentrations, imposed by the Freundlich model. If the value of  $n_S$  is equal to 1 then this equation will become a Langmuir equation. On the other hand, deviation of  $n_S$  value from the unity indicates heterogeneous surface. The linear expression is given in Equation 3.15, while the non-linear can be seen in Equation 3.16

$$\ln\left(\frac{Q_e}{Q_{max} - Q_e}\right) = \frac{1}{n_S} \ln C_e + \ln K_S \quad (3.15) \quad Q_e = \frac{K_S Q_m C_e^{1/n_S}}{1 + K_S C_e^{1/n_S}} \quad (3.16)$$

Where  $K_S$  is Sips isotherm model constant (L/g),  $n$  is isotherm exponent and  $Q_{max}$  is the maximum uptake of adsorbate. These parameters are dependent on pH, temperature and concentration.[45]

### 3.4.2 Adsorption kinetics

The pseudo-first order, or Lagergren's equation, and pseudo-second order models can be used to determine the adsorption kinetics. The adsorption capacity  $Q_t$  at time  $t$  (min) can be calculated using the following Equation 3.17

$$Q_t = \frac{(C_0 - C_t) * V}{m} \quad (3.17)$$

Where  $C_t$  (mg/L) is the dye concentrations at time  $t$  (min).

The models are based on equilibrium adsorption, and can be written as in Equation 3.18, for the first, and as in Equation 3.19, for the second.

$$\ln(Q_e - Q_t) = \ln Q_t - k_1 t \quad (3.18)$$

$$\frac{t}{Q_t} = \frac{1}{k_2 Q_e^2} + \frac{1}{Q_e} t \quad (3.19)$$

where  $Q_t$  is the amount of adsorbate adsorbed at an equilibrium time  $t$ , while  $k_1$  ( $\text{min}^{-1}$ ) and  $k_2$  ( $\text{g mg}^{-1} \text{min}^{-1}$ ) are the rate constants for the pseudo-first and -second order, respectively. The first order constant can be determined in linear form by plotting  $\ln(Q_e - Q_t)$  against  $t$ , whereas the second order can be determined by plotting  $\frac{t}{Q_t}$  against  $t$ . The fit of each model can be evaluated with the correlation coefficient  $R^2$ , which is calculated according to Equation 3.20

$$R^2 = 1 - \frac{\sum_{i=1}^n (y_i - \hat{y}_i)^2}{\sum_{i=1}^n (y_i - \bar{y}_i)^2} \quad (3.20)$$

where  $y_i$  are the experimental values,  $\hat{y}_i$  are the values estimated from the model, and  $\bar{y}_i$  are the mean values of  $y_i$ . Thus the closer  $R^2$  is to 1, the more accurate is the model for the kinetics of the adsorbent. [46] Many factors influence the adsorption capacity, such as the initial adsorbate concentration, the reaction temperature, the pH of the solution, the adsorbent particle size, and the nature of the solute. However, a kinetic model is concerned only with the effects on the overall rate. In general, it can be said that a pseudo-second-order rate equation describes the kinetics of a chemisorption process, whereas, a pseudo-first order describes the kinetics of a physisorption process.[47]

# 4 Methods & Experimental design

## 4.1 Synthesis of cage-like silsesquioxanes

### 4.1.1 Experimental considerations

The precursor for the synthesis of SQs T8 cages was APTES, which gives the possibility to post-functionalise the cages with simple organic chemistry reactions and allows for polymerisation when reacting with suitable monomer species. Acidic catalysis was preferred over alkaline because for an acidic process the hydrolysis and condensation steps will happen simultaneously, generating network-like gels, as stated in Section 3.1. Two types of acid catalysts were used to evaluate the influence of the catalyst as a function of time and on the type of product obtained. The first catalyst is Trifluoroacetic acid (TFA), selected from experimental works [19, 48] in which fluorinated catalysts were proven to give higher yields in less time, compared to other types of acid catalysts. Different ratios of APTES:TFA were explored to further investigate the influence of the pH on the final product. The second catalyst used was hydrochloric acid, which generally gives lower yields [19], however, given the stronger nature of the acid, it generates lower overall pH, which promotes ring-closure reactions, as stated in Section 3.1.3. The impact of the use of cosolvent was also examined, as it typically causes longer reaction times but is used to grant the miscibility of the system. Therefore, HCl catalysed reactions were attempted with and without cosolvent.

Cage cubic silsesquioxane structures with  $\text{NH}_3$  functionalities at the vertexes ([OAS-POSS-NH<sub>3</sub>]), shown in Figure 4.1, were synthesised following the experimental methods from Janeta et al. [19] and Kaneko et al. [48], varying the concentration of catalyst.

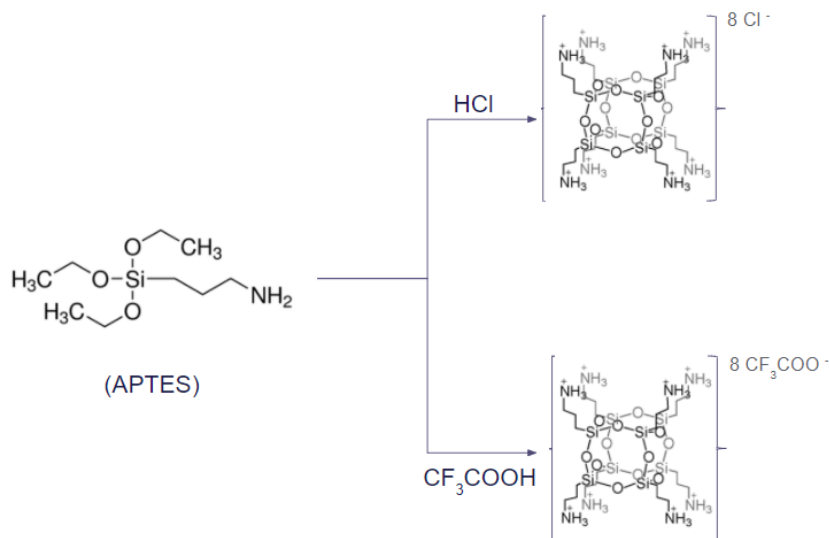


**Figure 4.1.** Schematic representation of the precursor and the catalysts used to obtain [OAS-POSS-NH<sub>3</sub>]

### 4.1.2 Procedure with trifluoroacetic acid as a catalyst

**Table 4.1.** List of chemicals used for the synthesis of [OAS-POSS-NH<sub>3</sub>] with TFA as a catalyst

Chemical	Specifications
(3-aminopropyl)triethoxysilane	Sigma-Aldrich, $\geq 98\%$ Lot # WXBC5326V, 919-30-2
Trifluoroacetic acid	Sigma-Aldrich, 99% Lot # T6508, 76-05-1
Acetone	VWR chemicals, 100% Lot # 21F114011, 67-64-1

A 250 mL double neck flask was equipped with a nitrogen purging outlet, an oil bath and a stirring magnet. An aqueous solution of trifluoroacetic acid was prepared by adding 2.30mL (30mmol) in a 100mL cylinder, and distilled water up to 68.4mL. Then, 3.51mL (15mmol) of (3-aminopropyl)triethoxysilane were set in the flask with a magnetic stirrer and the aqueous acid solution was added while keeping the solution under vigorous stirring. The thus made solution was mixed for 2 hours at room temperature after closing the system. The solution was then transferred to a plastic container and kept at 50°C for 2 hours to let the solvent evaporate. The crude product was then kept for 1 more hour at 100°C. Finally, the product was washed 4 times with 20mL of acetone, and vacuum dried (25°C, 0.5mbar).

This same procedure was repeated 3 additional times, varying the concentration of the acid catalyst solution so that the molar ratio between APTES:TFA would be 1:1.5, 1:3 and 1:4.

### 4.1.3 Procedure with Hydrochloric acid as a catalyst

**Table 4.2.** List of chemicals used for the synthesis of [OAS-POSS-NH<sub>3</sub>] SQs with HCl as a catalyst

Chemical	Specifications
(3-aminopropyl)triethoxysilane	Sigma-Aldrich, $\geq 98\%$ Lot # WXBC5326V, 919-30-2
Hydrochloric acid	Fisher chemical, 37% Lot#1901016, 7647-01-0
Methanol	VWR chemical, 100% Lot # 19J244018, 67-56-1

#### Ratio 1:3.6

A 500mL double neck flask was equipped with a nitrogen purging outlet, a water bath and a stirring magnet. To the thus prepared system were added 73mL of methanol, the stirring was then turned on, and 16mL of APTES were also added. While keeping a vigorous stirring 20mL of concentrated HCl were added, and the system was then closed. The system was then kept for 4 weeks at 25°C. After 4 weeks the product was washed with cold methanol and vacuum dried at 25°C and 0.5mbar. This procedure yielded crystals.

#### Ratio 1:0.01

A second procedure was attempted with HCl as a catalyst. A system made with an open plastic container with a stirring magnet and a water bath was prepared. To the container 6.1mL of water and 16mL of APTES were added, while maintaining a vigorous stirring. To the thus formed solution 55 $\mu$ L of concentrated HCl were added, and the plastic container was then capped with parafilm. The solution was left to react for 4 days at 50°C. After 4 days a gel product was formed, and left to age at room temperature for 72 hours. Finally

the product was dried in an oven at 110°C for 12 hours. This procedure yielded a glassy product.

## 4.2 Synthesis of TTSBI

### 4.2.1 Experimental considerations

For the synthesis of the organic part of the hybrid, as described in Section 3.2, the class of OMIMs was chosen to construct the organic part of the hybrid. A suitable monomer was selected based on chemical compatibility, rigidity, complexity of synthesis and purity of the final product. Therefore, TTSBI was chosen as the monomer. This molecule presents a rigid framework, shown in Figure 4.2, given by  $sp^2$  hybridised C, steric hindrance created by the methyl groups on the cyclopentane and -OH functional groups, that can be activated to react with the amine functionality, present on [OAS-POSS-NH<sub>3</sub>] cages. Furthermore, the synthesis of TTSBI consist in a single step reaction that yields a product with a purity of 98%, as reported from Lu et al. [49]

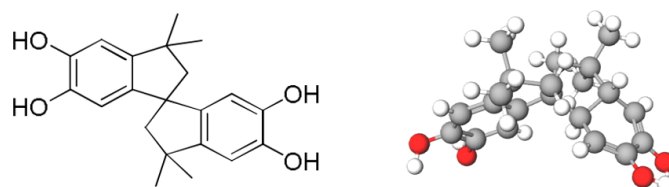


*Figure 4.2.* 2D and 3D representation of TTSBI. In the 3D figure, the red marked atoms represent oxygen atom, while the gray represent carbon and the white represent hydrogen.

### 4.2.2 Procedure

TTSBI was prepared following the synthesis from Lu et al. [49]

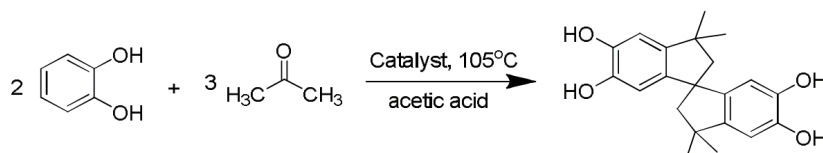


*Figure 4.3.* Reaction scheme for the synthesis of TTSBI with HBr as a catalyst [49]

**Table 4.3.** List of chemicals used for the synthesis of TTSBI with HBr as a catalyst

Chemical	Specifications
1,2-benzenediol	Sigma-Aldrich, 99%, 120-80-9
Hydrobromic acid	Sigma-Aldrich, 48% Lot #08021101, 10035-10-6
Acetone	VWR chemicals, 100% Lot # 21F114011, 67-64-1
Acetic Acid	Fisher chemical, 99.7% Lot#1999297, 64-19-7
Ethanol	VWR chemicals, Lot#22A0440, 64-17-5

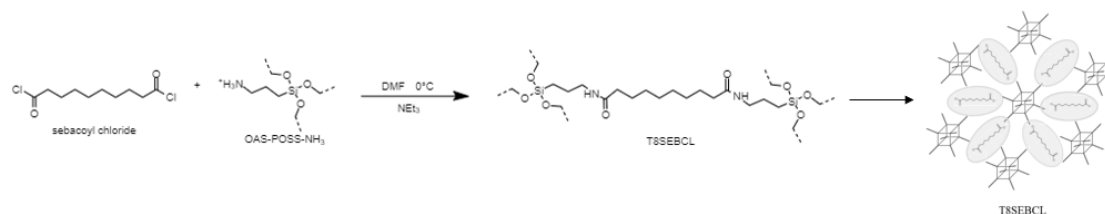
A 500mL double neck flask was equipped with a water condenser and an oil bath. To the flask, 50mL of acetic acid were added. Subsequently, 16.517g of 1,2-benzenediol, 16.65ml of acetone and 7mL of HBr were added to the previously prepared flask. The system was closed and set to react for 5 hours at 105°C. The product was then filtered, washed with acetic acid and recrystallised in ethanol. Finally the product was dried in an oven vacuum drier at 50°C and 0.5mbar for 24 hours.

### 4.3 Cross-linking between sebacoyl chloride and [OAS-POSS-NH<sub>3</sub>]

#### 4.3.1 Experimental considerations

This synthesis was performed, as a proof of concept, to compare the properties of a copolymer that contains T<sub>8</sub> SQ cages covalently bonded with a flexible hydrocarbon chain through an amide bond, with the properties of a copolymer between T<sub>8</sub> SQs cages covalently bonded to TTSBI, which is, by contrast, very rigid. Sebacoyl chloride was chosen because of the suitable length and flexibility of its structure, and because it is chemically compatible with the cage compound, given that acyl chlorides can easily react with amines, with the aid of a catalyst. The ratio was chosen to be 1:4.4 of OAS-POSS-NH<sub>3</sub> to sebacoyl chloride, as the first presents 8 functionalities, while the latter presents two functionalities. The catalyst chosen for this reaction was triethylamine (NEt<sub>3</sub>) as it was proven to be the most fit to avoid the degradation of the silsesquioxane cages. [19] The reaction was conducted under inert nitrogen atmosphere, to prevent sebacoyl chloride from reacting with atmospheric water, thus lowering the yield of the reaction, or eventually preventing the reaction from happening.

#### 4.3.2 Procedure

**Figure 4.4.** Reaction scheme between sebacoyl chloride and [OAS-POSS-NH<sub>3</sub>].

**Table 4.4.** List of chemicals used for the polymerisation of sebacoyl chloride and OAS-POSS-NH<sub>3</sub>

Chemical	Specifications
Sebacoyl chloride	Sigma-Aldrich, 111-19-3
Triethylamine	Sigma-Aldrich, 45% Lot # , 121-44-8
Hydrochloric acid	Fisher chemical, 37% Lot#1901016, 7647-01-0
Dimethylformamide (DMF)	VWR Chemicals, Lot#220516A005, 68-12-2
OAS-POSS-NH <sub>3</sub>	synthesised in section 4.1.3

A 500mL double neck flask was equipped with a nitrogen purging outlet, an ice bath and a stirring magnet. In the thus prepared system, a solution was prepared with 10mL of DMF and 0.0563g (0.0480mmol) of finely crushed OAS-POSS-NH<sub>3</sub>. The solution was stirred and 124μL (0.888 mmol, 18.5 equiv) of NEt<sub>3</sub> were added. Lastly, 45μL (0.2112mmol, 4.4 equiv) of sebacoyl chloride were added drop wise, and the system was capped and left to react overnight. The reaction yielded a white solid that was filtered and washed with 10mL of 1M HCl. Finally, the product was left to dry at room temperature overnight.

## 4.4 Cross-linking between TTSBI and random SQs structures

### 4.4.1 Experimental considerations

The synthesis was performed, as a proof of concept, to compare the properties of a copolymer between a rigid organic molecule, TTSBI, and a random, thus less rigid, silsesquioxane structure, with the completely rigid copolymer that would be formed by OAS-POSS-NH<sub>3</sub> and TTSBI. The reaction was conducted similarly to a sol-gel process, with HCl as a catalyst, as the integrity of the cages was not a concern. However, the solvent used was DMF, to grant the solubility of both reagents.

### 4.4.2 Procedure

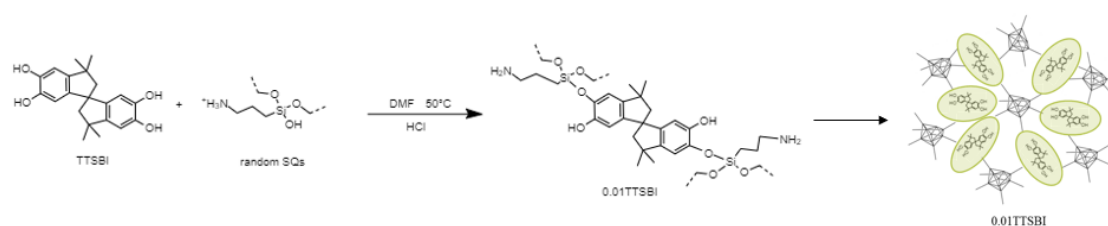


**Figure 4.5.** Reaction scheme between TTSBI and random SQs structures

**Table 4.5.** List of chemicals used for the condensation of TTSBI and incomplete OAS-POSS-NH<sup>3+</sup> cages

Chemical	Specifications
Hydrochloric acid	Fisher chemical, 37% Lot#1901016, 7647-01-0
Dimethylformamide	VWR Chemicals, Lot#220516A005, 68-12-2
OAS-POSS-NH <sub>3</sub>	synthesised in section 4.1.3
TTSBI	synthesised in section 4.2

A 500mL double neck flask was equipped with an oil bath and a condenser, on a stirring plate. In the flask, a solution was prepared with 10mL of DMF and 0.0563g (0.0480mmol) of finely crushed OAS-POSS-NH<sub>3</sub>. The solution was stirred and 14.2μL (0.172 mmol, 3.6 equiv) of HCl were added. Lastly, 0.0572g (0.1680mmol, 3.5 equiv) of TTSBI were added drop wise, and the system was capped and left to react overnight. The reaction yielded a white solid that was filtered and washed with 10mL of 1M HCl. Finally, the product was left to dry at room temperature overnight.

## 4.5 Cross-linking between TTSBI and [OAS-POSS-NH<sub>3</sub>]

### 4.5.1 Experimental considerations

Before reacting with the OAS-POSS-NH<sub>3</sub>, TTSBI was oxidised to turn the molecule in a  $\alpha,\beta$ -unsaturated carboxylic acid derivative. To do so, a mild oxidation with 2-Iodoxybenzoic acid (IBX) was performed, following the protocol from Magdziak et al. [50]. The final bond between the two molecules results in a secondary amine, which is a stable bond in aqueous conditions. Because of the scarce solubility of the two monomers, the reaction is conducted in DMF, and the catalyst used is NEt<sub>3</sub>, as stronger bases could damage the T8 structure. The ratio between OAS-POSS-NH<sub>3</sub> and TTSBI is 1:4.4, as the T8 structure presents 8 functionalities, and the expected oxidised TTSBI would present 4 functionalities, of which at least 2 are expected to react.

### 4.5.2 Procedure

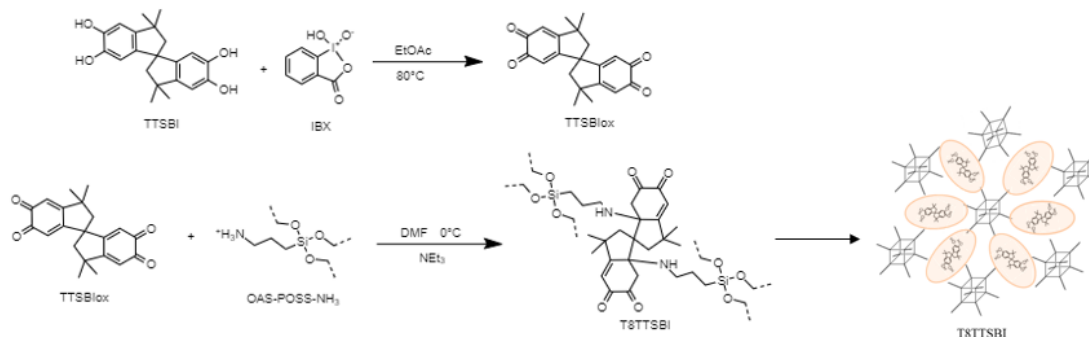


**Figure 4.6.** reaction scheme between OAS-POSS-NH<sub>3</sub> and oxidised TTSBI.

**Table 4.6.** List of chemicals used for the polymerisation of TTSBI and OAS-POSS-NH<sub>3</sub>

Chemical	Specifications
TTSBI	synthesised in section 4.2
Triethylamine	Sigma-Aldrich, 45%, 121-44-8
Dimethylformamide	VWR Chemicals, Lot#220516A005, 68-12-2
Ethyl Acetate (EtOAc)	VWR Chemicals, Lot#200420A006, 141-78-6
OAS-POSS-NH <sub>3</sub>	synthesised in section 4.1.3

### TTSBI oxidation

A 500mL double neck flask was equipped with an oil bath and a condenser, on a stirring plate. A solution with 4.22mL of EtOAc and 0.07189g (0.2112mmol) of TTSBI was prepared in the flask. After complete dissolution of TTSBI, 0.1774g (0.6336mmol, 3 equiv) of IBX were added, and the solution was left to react with stirring for 4 hours at 80°C. The solution was then cooled at room temperature and filtered with a paper filter to extract the IBX. The liquid filtrate was then evaporated with a rotary evaporator to eliminate the solvent and leave oxidised TTSBI as a dark brown powder.

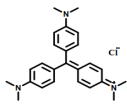
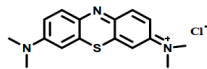
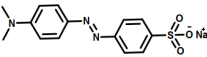
### Aza-michael's addition

A 500mL double neck flask was equipped with an ice bath on a stirring plate. In the flask, a solution was prepared with 10mL of DMF, 0.0563 g (0.0480 mmol) of OAS-POSS-NH<sub>3</sub> and NEt<sub>3</sub> 0.124 mL (0.888 mmol, 18.5 equiv). Once the OAS-POSS-NH<sub>3</sub> was dissolved, 0.07189 g (0.2112 mmol, 8.8 equiv) of TTSBI were added, and the solution was left to react overnight with stirring. The reaction yielded a solid that was filtered and washed with 10mL of 1M HCl. Lastly, the product was left to dry at room temperature overnight.

## 4.6 Dye & heavy metal ion adsorption experiments

Adsorption experiments were determined by batch method, in which a fixed amount of the adsorbent (5mg) was added to 15mL of dye aqueous solution, for Methylene Blue (MB) and Methyl orange (MO), and 25mL for Crystal violet (CV) of varying concentrations taken in sealed flasks. A total of 8 different initial concentrations were prepared, in a range between 5mg/L and 400mg/L.

**Table 4.7.** Physical and chemical properties of dyes.

Dye	Molecular structure	Molecular size (nm)	Molecular weight (g/mol)	Nature	Adsorption wavelength (nm)
CV		1.41*1.21*0.18	407	cationic	590 [29]
MB		1.26*0.77*0.65	320	cationic	665 [29]
MO		1.31*0.55*0.18	327	anionic	465 [29]

The experiment was repeated for each hybrid synthesised in Sections 4.4, 4.5 and 4.3. The initial concentration was determined with UV/Vis absorption, and the equilibrium concentration was measured after the solutions were left with moderate stirring at RT for 24h. The amount of dye adsorbed was calculated based on Equation 3.7. The same experiment was repeated for each hybrid with solutions of Nickel(II) chloride (NiCl<sub>2</sub>\*6H<sub>2</sub>O) in a range of concentrations between 5mg/L and 90mg/L. After having determined the adsorption capacity, a kinetic experiment was performed by using 10mg of the adsorbents in an aqueous solution with a CV concentration of 10mg/L, where the concentration of

the solution was monitored at different time intervals with UV/Vis spectrometry. The adsorption capacity at time  $t$  (min) was calculated following Equation 3.17.

Finally, a cyclic adsorption/regeneration test was performed in an aqueous solution of 10mg/L of dye and 10mg of adsorbent. The adsorbent was then regenerated by washing with hot methanol at 50°C with light stirring, and then washing with distilled water.

## 4.7 Analysis

The products synthesised were analysed with attenuated total reflection FTIR (ATR-FTIR), nuclear magnetic spectroscopy (NMR), thermogravimetric analysis (TGA). The concentration of the dye and heavy metal solutions were measured, respectively, with Ultraviolet/Visible (UV/Vis) spectroscopy and Atomic absorption spectroscopy (AAS).

### 4.7.1 ATR-FTIR

FTIR measurements were carried out in an infrared spectrometer ATR-FTIR Bruker on a transmission mode. Spectra were collected in the range 400 to 4000  $\text{cm}^{-1}$  at 2  $\text{cm}^{-1}$  resolutions with 64 scans. After the measurement, operations of min-max normalization and base-line correction were done as a post treatment with the program OPUS. This analysis was done in order to assess the presence of certain functional groups.

### 4.7.2 NMR

NMR spectra were carried out with Bruker NMR spectrometers and analysed with the software Topspin. This technique was used, principally, to identify the structure of the precursors, as this analysis is based on resonance.

### 4.7.3 TGA

All the TGA measurements were carried out on a Discovery SDT 650 with a temperature ramp of 10 °C/min to 1000 °C. For this project, this technique was used to determine the thermal stability of the materials, by identifying the temperature of decomposition ( $T_d$ ). [51]

### 4.7.4 UV/Vis & AAS

All the adsorption isotherm for dye adsorption experiments were obtained from UV/Vis absorbance measurements carried on a Varian Cary 50 UV-Vis Spectrophotometer, in a wavelength range of 300-800nm. The scan rate was of 24000 nm/min, and the data interval was of 5nm. The data points reported in the isotherms are selected from the wavelength of maximum absorbance of each dye, which are 590nm for CV, 465nm for MO and 665nm for MB. For the adsorption profiles of Ni, the solutions were measured with AAS at the wavelength of 232nm, with each concentration averaged over 5 measurements.

Computer technology has enabled the use of nonlinear optimization methods as an alternative to linearization to determine isotherm parameters. As the data is not transformed in this method, there is no distortion of error distributions, making this distribution more representative of the actual errors in the data. Furthermore, comparisons

of linear and nonlinear regressions have shown that the best parameter estimates were returned by nonlinear fitting. [52] For the above stated reasons, the adsorption isotherms were analyzed according to the nonlinear form of Langmuir, Freundlich, Sips and Jovanovic models, respectively shown in Equation 3.9, 3.14, 3.16 and 3.12.

The accuracy of the fit was estimated through the correlation coefficient  $R^2$ , which was calculated as in Equation 3.20.

# 5 Results & Discussion

## 5.1 Analysis of SQ structures from HCl catalysis

The procedure with HCl as a catalyst with the molar ratio of APTES:HCl was 1:0.01 yielded a white powder product, with a quantitative yield of 62.4% calculated on the ideal chemical formula of one unit of product as  $[\text{SiO}_{1.5}(\text{CH}_2)_3\text{NH}^{3+}\text{Cl}^-]$ . An ATR-FTIR spectra was performed on the product, shown in Figure 5.1 (A). Peaks showed an Si-O-Si stretching adsorption band at  $1005\text{ cm}^{-1}$  and  $1099\text{ cm}^{-1}$  which could indicate that the product formed is not a cage, given that the cubic compounds is highly symmetrical and generally gives only one relatively narrow signal. [48] At  $1597\text{ cm}^{-1}$  a signal for the  $\text{NH}^{3+}$  can be seen.

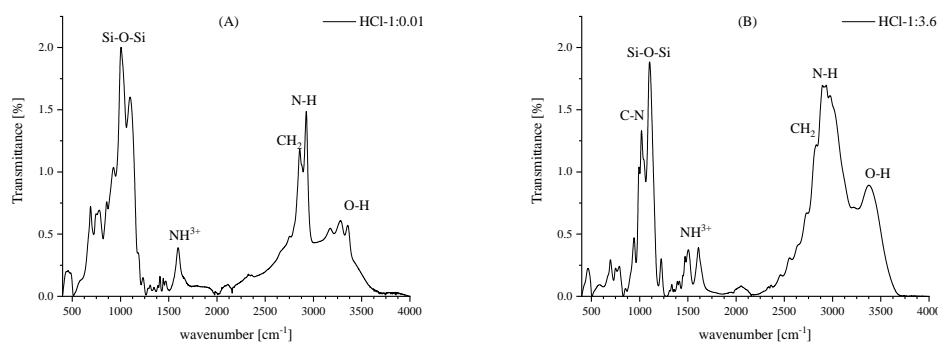


**Figure 5.1.** ATR-FTIR spectra of products obtained from the synthesis method employing HCl as a catalyst with a molar ratio of 1:0.01 (A) and 1:3.6 (B) of APTES:HCl.

Figure 5.1 (B) shows the spectrum resulting from the procedure with the molar ratio of APTES:HCl of 1:3.6, which yielded a white powder, with a quantitative yield of 25.5% calculated on the ideal chemical formula of one unit of product as  $[\text{SiO}_{1.5}(\text{CH}_2)_3\text{NH}^{3+}\text{Cl}^-]$ . The Si-O-Si stretching band is narrow, however around  $1020\text{ cm}^{-1}$  a peak for primary amine C-N stretching can be seen; furthermore, at  $3400\text{ cm}^{-1}$  a signal for the O-H of a primary alcohol is present, indicating that the cage product was possibly formed but some of the functionalities did not react. Both figure (A) and (B) show a peak around  $3000\text{ cm}^{-1}$  for the N-H stretching of a primary amine. [19]

$^1\text{H}$  NMR and decoupled  $^{13}\text{C}$  NMR spectra of the obtained SQs products were measured in deuterated dimethyl sulfoxide (DMSO-D6) to investigate the structure. The sample with 1:3.6 molar ratio of APTES:HCl showed close resemblance to the literature, as the peaks, reported in Table 5.1, correspond to the ones found from Janeta et al. [19]. The spectra are shown in Figure 5.2

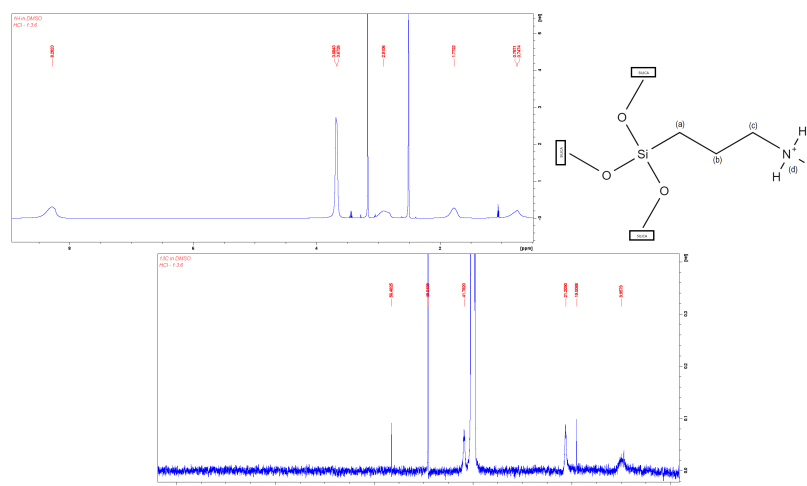


**Figure 5.2.**  $^1\text{H}$  NMR and decoupled  $^{13}\text{C}$  NMR spectra of product obtained from the synthesis method employing HCl as a catalyst with a molar ratio of 1:3.6 for APTES:HCl

For the 1:3.6 sample, the peaks that denote the formation of the cages are at 41.78ppm (c), 21.21ppm (b), 9.69ppm (a) for the  $^{13}\text{C}$  NMR, and at 8.28ppm (d), 2.91ppm (c), 1.77ppm (b), 0.74ppm (a) for the  $^1\text{H}$  NMR. [19] As for the previous sample, the more shielded signals are given by the atoms closer to the silica cage, while the less shielded signal are given by the atoms closer to the protonated amine group. Additionally, peaks related to unreacted hydroxy groups from the precursor show at 3.68ppm in the  $^1\text{H}$  NMR and at 56.48ppm and 19.00ppm in the  $^{13}\text{C}$  NMR.

**Table 5.1.**  $^1\text{H}$  NMR and decoupled  $^{13}\text{C}$  NMR decoupled data from samples measured in DMSO

sample	$^1\text{H}$ NMR	$^{13}\text{C}$ NMR
	( $\text{NH}^{3+}$ ), ( $\text{CH}_2\text{NH}^{3+}$ ), ( $-\text{CH}_2-$ ), ( $\text{SiCH}_2$ )	( $\text{CH}_2\text{NH}^{3+}$ ), ( $-\text{CH}_2-$ ), ( $\text{SiCH}_2$ )
1:3.6	3.68 ( $\text{OH}-\text{H}_2\text{O}$ ), 8.28, 2.91, 1.77, 0.74	41.78, 21.21, 9.69, 56.48 ( $\text{CH}_3\text{CH}_2\text{O}-$ ), 19.00 ( $\text{CH}_3\text{CH}_2\text{O}-$ )

The sample with molar ratio 1:0.01 of APTES:HCl, displayed in Figure 5.3 doesn't show any significant peaks in the  $^{13}\text{C}$  NMR, given the scarce solubility of the product. In  $^1\text{H}$  NMR the peaks presented are not characteristic of the cubic  $\text{T}_8$  structure, suggesting that the network formed is random. The two intense peak are due to DMSO-D<sub>6</sub> at 2.50ppm, and to moisture in the solvent at 3.33ppm. It is also to be noted that this product was scarcely soluble in DMSO-D<sub>6</sub>.

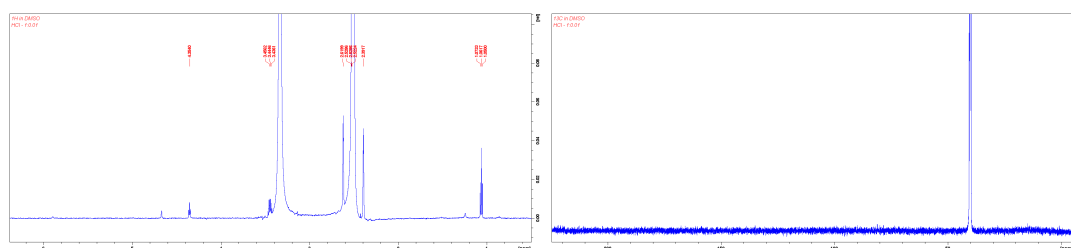


**Figure 5.3.**  $^1\text{H}$  NMR and decoupled  $^{13}\text{C}$  NMR spectra of product obtained from the synthesis method employing HCl as a catalyst with a molar ratio of 1:0.01 for APTES:HCl

## 5.2 Analysis of SQ structures from TFA catalysis

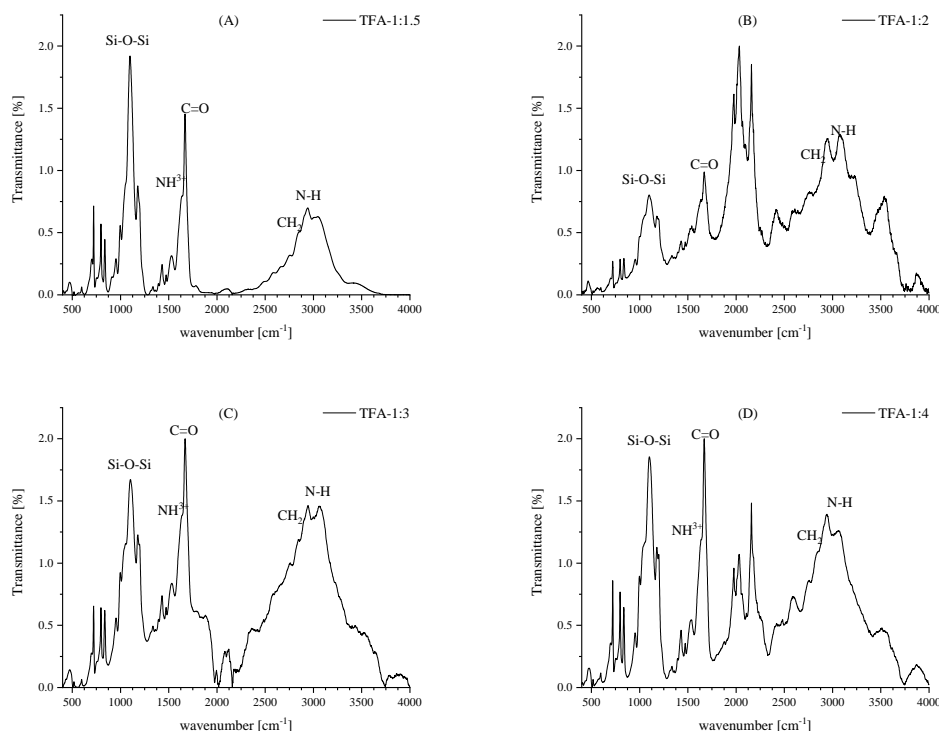


**Figure 5.4.** ATR-FTIR of products obtained from the synthesis method employing TFA as a catalyst with a molar ratio of APTES:TFA of 1:1.5 (A), 1:2 (B), 1:3 (C), and 1:4 (D).

When TFA was used as a catalyst, with a molar ratio 1:1.5 of APTES:TFA, it yielded a transparent flexible material, with a quantitative yield of 85.5% calculated on the ideal chemical formula of one unit of product as  $[\text{SiO}_{1.5}(\text{CH}_2)_3 \text{NH}^{3+} \text{CF}_3\text{COO}^-]$ . The Si-O-Si stretching band, shown in Figure 5.4 (A), looks narrow, and there are no significant peaks for unreacted hydroxy groups. The peak for  $\text{NH}^{3+}$  peak was merged with the C=O stretching signal which also occurs around  $1600 \text{ cm}^{-1}$  [48]. In the area between  $2600 \text{ cm}^{-1}$  to  $3000 \text{ cm}^{-1}$  signals for C-H stretching of a secondary C can be seen, as well as N-H stretching of primary amine around  $3000 \text{ cm}^{-1}$ . [19] However, only the 1:1.5 molar ratio shows peaks relative to the expected  $\text{T}_8$  cubic compound, given that the other ratios, shown in Figures 5.4 (B), (C) and (D), present large Si-O-Si bands, and relative higher transmittance of C-H for secondary C.

$^1\text{H}$  NMR and decoupled  $^{13}\text{C}$  NMR spectra for the product obtained from 1:1.5 molar ratio of APTES:TFA showed the closest resemblance with literature, with good correspondence between the peaks reported from Janeta et al. [19] and the ones reported in this work in Table 5.2. The spectra are shown in Figure 5.5.

**Table 5.2.**  $^1\text{H}$  NMR and decoupled  $^{13}\text{C}$  NMR decoupled data from samples measured in DMSO

sample	$^1\text{H}$ NMR ( $\text{NH}^{3+}$ ), ( $\text{CH}_2\text{NH}^{3+}$ ), ( $-\text{CH}_2-$ ), ( $\text{SiCH}_2$ )	$^{13}\text{C}$ NMR ( $\text{CH}_2\text{NH}^{3+}$ ), ( $-\text{CH}_2-$ ), ( $\text{SiCH}_2$ )
1:1.5	7.67, 2.81, 1.59, 0.55	41.73, 20.83, 8.41, 161.47 ( $\text{CF}_3\text{COO}^-$ ), 117.37 ( $\text{CF}_3\text{COO}^-$ )

For the 1:1.5 sample, the peaks that denote the formation of the cages are at 8.41 ppm (a), 20.83ppm (b) and 41.73ppm (c) for the  $^{13}\text{C}$  NMR, and at 7.67ppm (d), 2.81ppm (c), 1.59ppm (b), 0.55ppm (a) for the  $^1\text{H}$  NMR. [19] The less shielded signal in  $^{13}\text{C}$  NMR is given by the C atom closer to the protonated amine group, while the more shielded signal is given by the C atom that bonds with the Si atom of the  $\text{T}_8$  cage. The same happens for the  $^1\text{H}$  NMR signals.

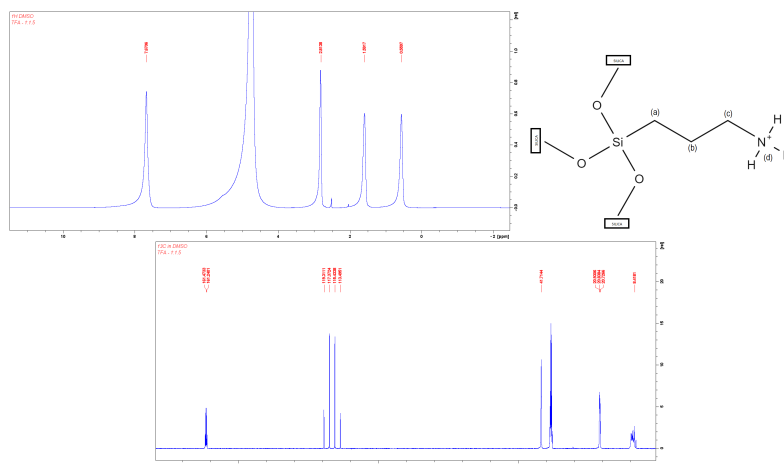


**Figure 5.5.**  $^1\text{H}$  NMR and decoupled  $^{13}\text{C}$  NMR spectra of product obtained from the synthesis method employing TFA as a catalyst with a molar ratio of 1:1.5 for APTES:TFA

$^1\text{H}$  NMR spectra were measured also for the samples with different ratio of APTES:TFA for comparison. In Figure 5.6 the peaks around 1.5ppm, 2.8ppm and 7.7ppm characteristic of the cages show, however the peak at 0.5ppm is barely observable, and an additional peak around 2.5ppm appears in all the samples

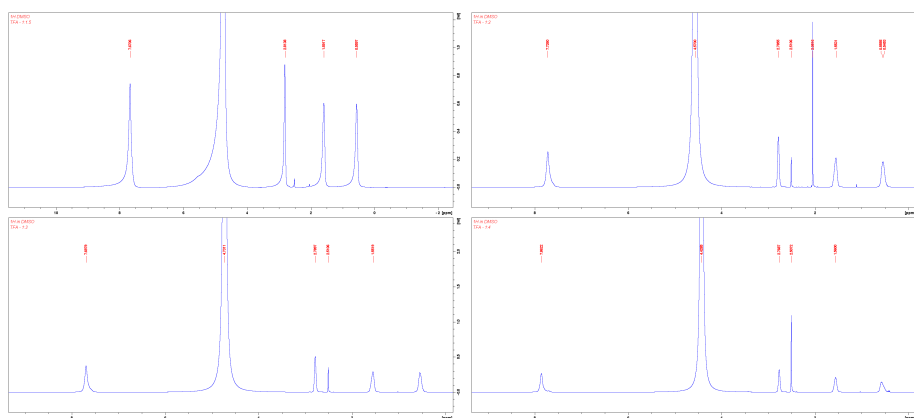


**Figure 5.6.**  $^1\text{H}$  NMR spectra of product obtained from the synthesis method employing TFA as a catalyst with a molar ratio of 1:2, 1:3 and 1:4 for APTES:TFA

### 5.3 NMR analysis of TTSBI

$^1\text{H}$  NMR analysis was also performed on TTSBI, to investigate the formation of the desired structure.

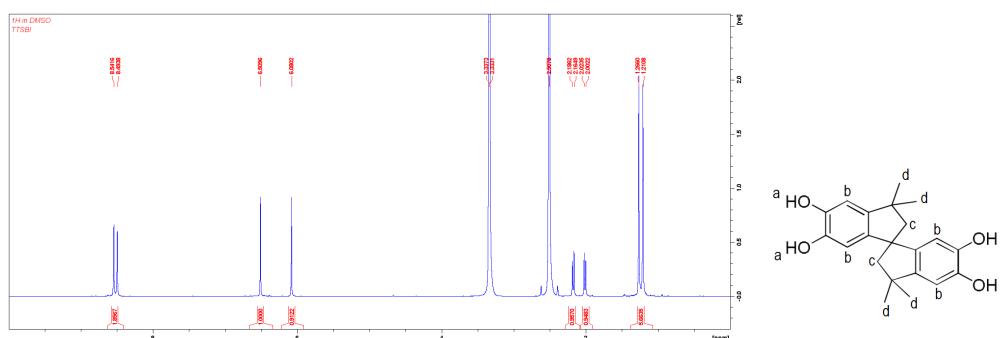


**Figure 5.7.**  $^1\text{H}$  NMR spectrum of TTSBI

The peaks shown in Figure 5.7 correspond to the ones obtained by Lu et al. [49]. In particular, the peaks at 8.54ppm and 8.49ppm correspond to the hydrogen (a) from the alcohol groups on the benzene rings, the peaks at 6.50ppm and 6.08ppm correspond to the hydrogen(b) next to the -OH groups on the benzene rings. The peaks at 2.19ppm, 2.16ppm, 2.02ppm and 2.00ppm correspond to the hydrogen(c) on the pentane ring, while the peaks at 1.26ppm and 1.21ppm correspond to the hydrogen(d) on the methyl substituents on the pentane ring. The integrated peaks show further correspondence between the expected structure and the signals, as the integration shows how the structure is specular, hence giving 1 for all the signals besides the one belonging to (c), which is generated by 6 H on each specular side of the molecule. Peaks at 2.50ppm and 3.33ppm are, respectively, due to the solvent peak, DMSO-D<sub>6</sub>, and due to moisture present in the solvent.

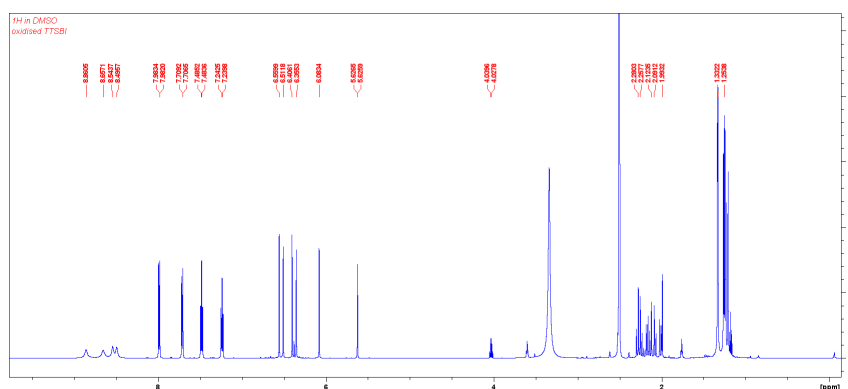


**Figure 5.8.**  $^1\text{H}$  NMR spectrum of oxidised TTSBI

The oxidised spectra of TTSBI, in Figure 5.8, presents peaks around 1.25ppm, 2.09ppm and 2.12ppm for, respectively, the hydrogen on the methyl substituent, and the hydrogen on the pentane ring, as the untreated version. However the peaks appear to be more split and asymmetrical, compared to untreated TTSBI. A multitude of peaks between 6.55ppm and 5.62ppm could be ascribed to the hydrogen present on the conjugated structure of the rings, while the far left peak between 8.86ppm and 7.23ppm could be generated by hydrogen close to the carbonyl or on the oxygen adjacent to the carbonyl. The high number of signals could be due to the incomplete oxidation of TTSBI.

## 5.4 Analysis of hybrids

From the monomers above analysed, and synthesised in Section 4.1.3 and 4.2, a total of three hybrids was made, of which the structures can be seen in Figure 5.9. Despite the higher yield and purity of silsesquioxanes cage-like structures obtained with TFA as a catalyst, the T<sub>8</sub>-SQs used for these modifications were the ones obtained with HCl catalysis. This is due to the fact that TFA catalysis yielded glassy products, hence hard to handle and weigh, whereas HCl catalysis yielded powder products. Furthermore, the expected properties from the two different catalysis should not change drastically, as they form the same final structure.

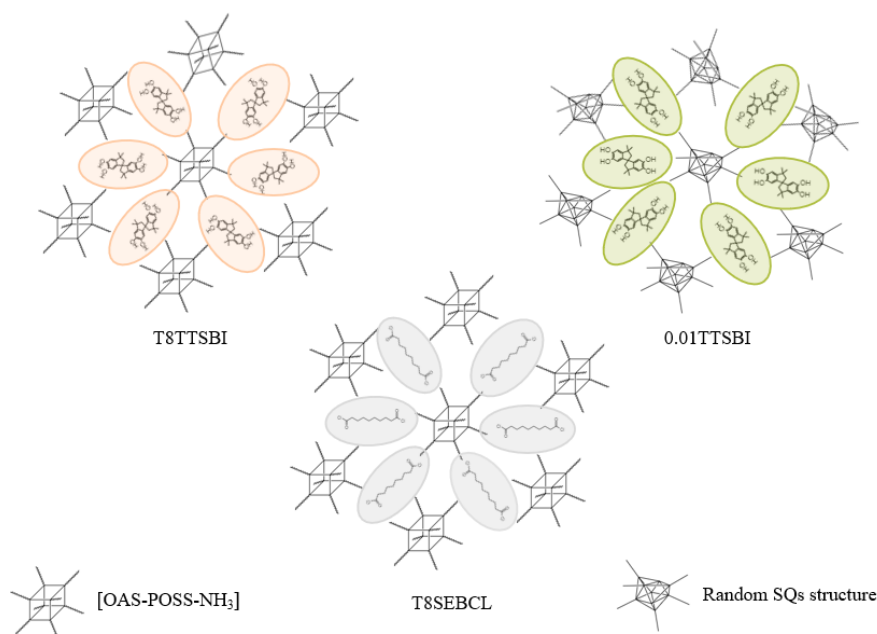


**Figure 5.9.** Expected chemical structure of the hybrids synthesised in Section 4.4, 4.5 and 4.3

The hybrids obtained resulted in fine powders, for 0.01TTSBI and T<sub>8</sub>TTSBI, and in a dense white liquid for T<sub>8</sub>SEBCL. The yields were of 18% for 0.01TTSBI, 30% for T<sub>8</sub>TTSBI and 20% for T<sub>8</sub>SEBCL, calculated on the ideal chemical formula of one unit of product respectively as [SiO<sub>1.5</sub>(CH<sub>2</sub>)<sub>3</sub>NH<sub>2</sub>C<sub>21</sub>H<sub>22</sub>O<sub>2</sub>] for 0.01TTSBI, as [SiO<sub>1.5</sub>(CH<sub>2</sub>)<sub>3</sub>NHC<sub>21</sub>H<sub>24</sub>O<sub>4</sub>] for T<sub>8</sub>TTSBI, and [SiO<sub>1.5</sub>(CH<sub>2</sub>)<sub>3</sub>NHC<sub>10</sub>H<sub>16</sub>O<sub>2</sub>] for T<sub>8</sub>SEBCL.

All the FTIR spectra of the hybrids present peaks both in the low wavelength region, typical of inorganic compounds, and in the high wavelength region, typical of organic compounds.

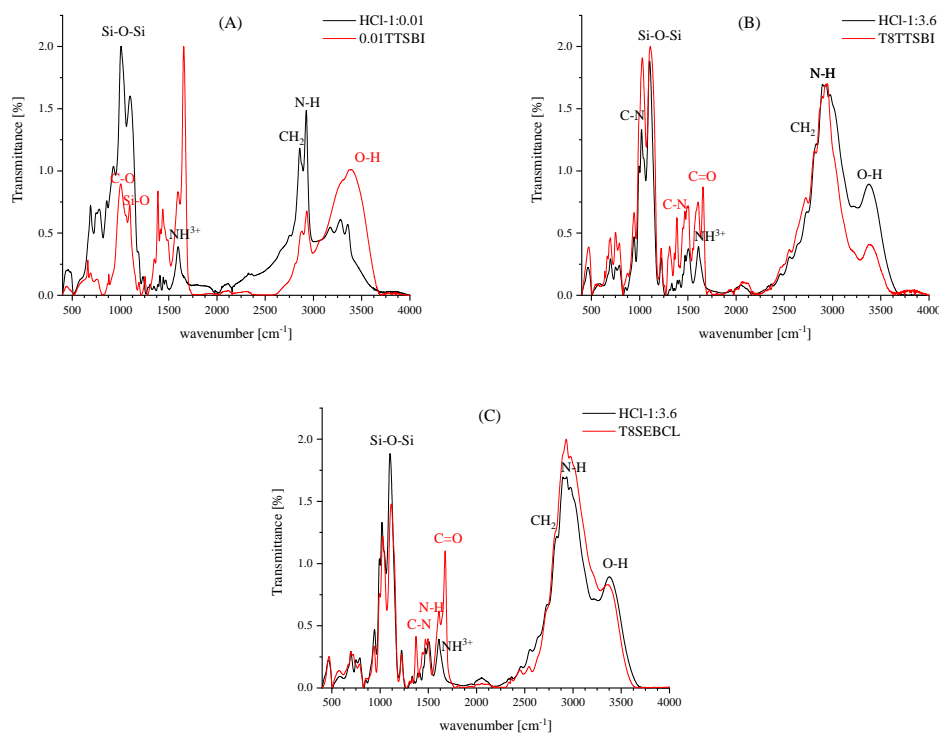


**Figure 5.10.** ATR-FTIR spectra for the SQs precursors (black line) and the post modified product (red line) of the reactions between open silsesquioxane random structures with TTSBI (A), OAS-POSS-NH<sub>3</sub> with oxidised TTSBI (B), and OAS-POSS-NH<sub>3</sub> with sebacoyl chloride (C).

The spectra for 0.01TTSBI, in Figure 5.10 (A), presents still N-H and CH<sub>2</sub> peaks, while it presents a broad phenolic O-H adsorption band at 3373 cm<sup>-1</sup>, which can indicate that not all the -OH functionalities of TTSBI have reacted, probably due to steric hindrance. The Si-O-C bond appears in the wavenumber range between 950 and 1150 cm<sup>-1</sup>, and consists of the C-O and Si-O bonds. [53] A group of signals typical of catechol show in the region between 1400 and 1650 cm<sup>-1</sup>, due to the C=C vibration of the aromatic ring. [54]

The resulting spectra for T8TTSBI, shown in Figure 5.10 (B), presents the same peaks for the the SQs structure, as the red line and the black line overlap for the Si-O-Si bond region, whereas it presents a range of peaks in the region between 1400 and 1650 cm<sup>-1</sup> for the red line, which can be ascribed to the modification done by the oxidised TTSBI molecules. Therefore peaks for C=C vibration of the aromatic ring can be seen. [54]

For the spectra of T8SEBCL, which can be seen in Figure 5.10 (C), signals for N-H, C-N and C=O stretching can be seen, which indicates the formation of the desired amine bond, as reported from Mateusz et al. [19]. Furthermore, the signals for the cage structures correspond between the pre- and post-modification, therefore the structure was not altered.

<sup>1</sup>H NMR analysis was performed on the synthesised hybrids. However, the obtained spectra could not give much significant information, as the structures formed are quite complex and the solubility of the hybrids was scarce in the NMR solvent.

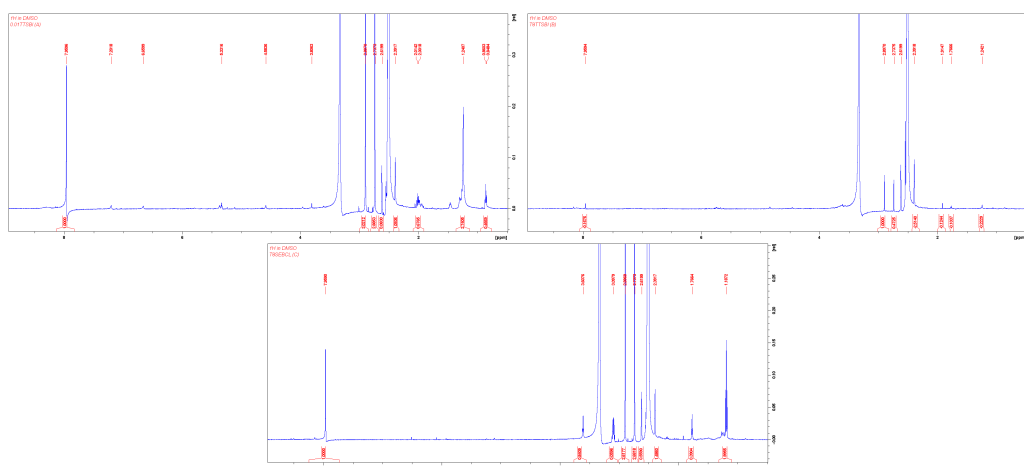


**Figure 5.11.**  $^1\text{H}$  NMR and decoupled  $^{13}\text{C}$  NMR spectra of product obtained of the reactions between open silsesquioxane random structures with TTSBI (A), OAS-POSS-NH<sub>3</sub> with oxidised TTSBI (B), and OAS-POSS-NH<sub>3</sub> with sebacyl chloride (C).

## 5.5 Thermal stability of hybrids

The profiles for 0.01TTSBI and T8SEBCL, respectively in Figure 5.12 (A) and (C), show an initial step decrease, ascribable to the weight loss from small solvent molecules, or oligomers present in the organic part of the samples.

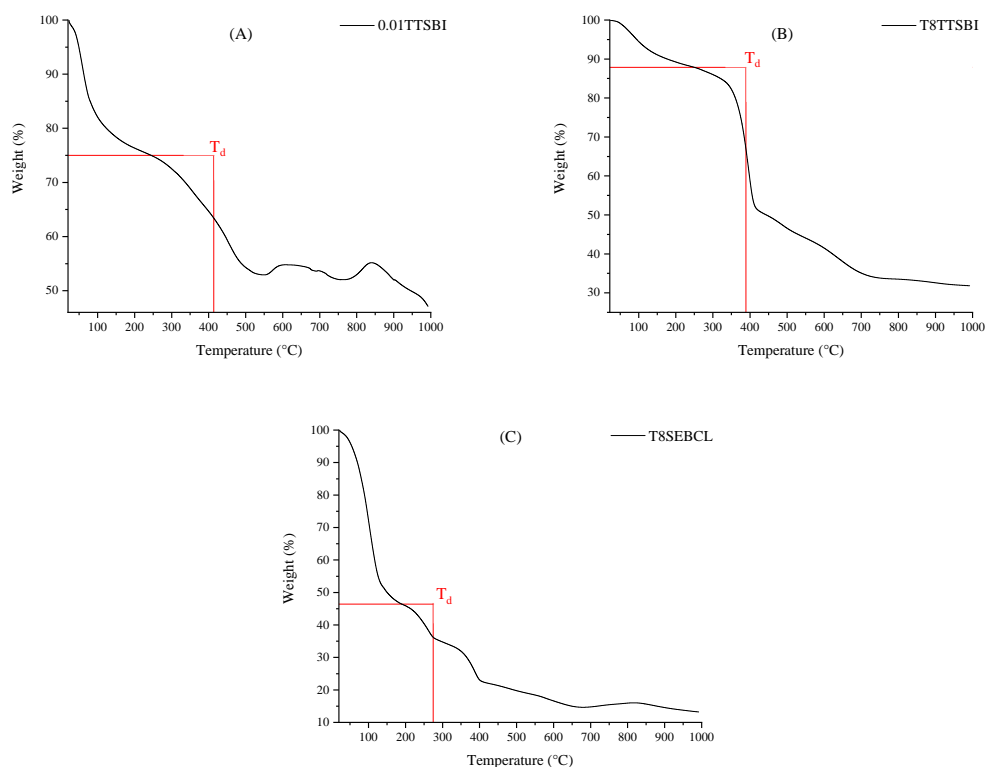


**Figure 5.12.** TGA curve of 0.01TTSBI (A), T8TTSBI (B), and T8SEBCL (C).

The  $T_d$  for 0.01TTSBI is of 413.07°C, and the decomposition interval appears to be broad, which can be expected from the presence of different kind of silica structures, due to the

formation of random SQs in the sol-gel process. After decomposition, the mass stays around 50%, due to the presence of Si-O-Si networks, which have a high thermal stability and therefore do not decompose. [55] For T8SEBCL two consecutive decreases can be observed, which could be due to the presence of open cage and closed cages  $T_8$  cages, or to different overall structure formations during the networking process. The  $T_d$  is identified in the first decrease at  $274.82^\circ\text{C}$ . In this case, the weight% reaches around 15 and stops decreasing, for the presence of Si-O-Si networks. The profile for T8TTSBI, in Figure 5.12 (B), unlike the other two hybrids, shows a very small loss of weight initially, likely due to small molecules of solvent. This behaviour can be attributed to the presence of a better organic network, hence the formation of a polymeric shell of TTSBI around the T8 core of SQs cages. The  $T_d$  is of  $388.68^\circ\text{C}$ , which is lower than 0.0TTSBI, probably due to the more polymeric inorganic structure of random SQs. Furthermore, the decomposition curve is more defined compared with the profile in Figure 5.12 (A) and (B), indicating a more regular structure. The ending plateau for T8TTSBI is reached at  $800^\circ\text{C}$  with a 35% of weight left, which differs from T8SEBCL, although the silica structure for the two hybrids is expected to be equal.

## 5.6 Adsorption isotherms

The results for the adsorption of MB onto the 3 hybrids are shown in Figure 5.13, where all the isotherms display the same profile.

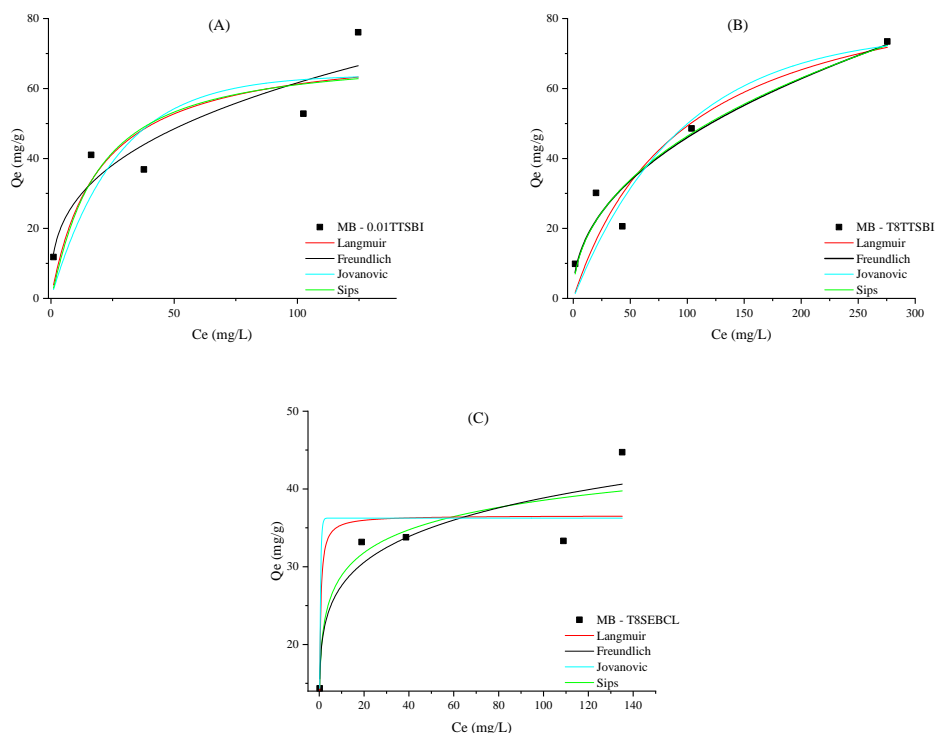


**Figure 5.13.** The Langmuir (red line), Freundlich (black line), Jovanovic (cyan line) and Sips (green line) non-linear isotherm model fitted on initial different concentrations of MB onto 0.01TTSBI (A), T8TTSBI (B) and T8SEBCL (C).

These curves shape are due to strong driving force between the liquid/solid phases, which are present when the concentration of the dye is higher in the solution than in the adsorbent. [46] Therefore the profiles present an increase in the amount adsorbed at low concentrations, when the ratio between the available binding sites to the initial dye concentrations is large. The curves then reach a plateau at higher concentrations, when the saturation of the adsorption sites occurred.

For MB adsorption, the  $R^2$  values, in Table 5.3, show that the Freundlich model is the best fit for the adsorption behaviour of 0.01TTSBI and T8TTSBI, with the respective values of 0.86 and 0.92. This indicates that the surface of the adsorbents is heterogeneous, thus surface adsorption sites are energetically heterogeneous and the process is reversible. The  $K_F$  and  $n_F$  parameters have a higher value for the adsorbent 0.01TTSBI, which could give an indication on the relative size for pores of the material, as the adsorbent T8TTSBI is expected to have smaller pore size compared to 0.01TTSBI. This is given by the rigid small structure of T8 SQs cages, which, as mentioned in, Section 2.2, tend to generate molecules with diameters ranging from 1 to 3 nm, and OMIMs tend to generate interconnected pores of 2nm diameter. Given that 0.01TTSBI forms random SQs structures, it is to be expected that a molecule such as MB, with a molecular size of  $1.26 \times 0.77 \times 0.65$ nm, will adsorb better on a the adsorbent with a greater pore size.

It is to be noted that, the  $R^2$  values of the Freundlich and the Sips models for T8TTSBI give the same accuracy. This could indicate that the adsorption of T8TTSBI for MB conforms to both adsorption models. Nonetheless, Sips model accounts for the limitation of the Freundlich model at high concentrations, predicting a monolayer formation according to Lngmuir model. This could indicate that once the small pores of the adsorbent are filled, the remaining dye tends to accumulate on the formed adsorbate-adsorbent system, probably due to favourable chemical interactions, given by the  $\pi - \pi$  stacking of the conjugated planar structure in MB and the C=O bonds in the adsorbent. Ionic interactions could also be playing a role, between the positively charged N atoms on the dye and the electron rich C=O bond on the oxidised TTSBI.

**Table 5.3.** Summary of Langmuir, Freundlich, Sips and Jovanovic isotherm model parameters for the adsorption of MB on 0.01TTSBI, T8TTSBI and T8SEBCL.

Adsorbent in MB	Langmuir			Freundlich			Sips				Jovanovic		
	$Q_m$ (mg/g)	$K_L$ (L/mg)	$R^2$	$K_F$ (L/g)	$n_F$	$R^2$	$Q_m$ (mg/g)	$K_S$ (L/mg)	$n_S$	$R^2$	$Q_{max}$	$K_J$ (L/mg)	$R^2$
0.01TTSBI	72.99	0.05	0.77	12.48	2.88	0.86	69.90	0.04	0.90	0.76	63.90	0.04	0.72
T8TTSBI	96.96	0.01	0.86	5.80	2.22	0.92	642.84	0.01	2.07	0.92	76.28	0.01	0.85
T8SEBCL	36.59	2.91	0.81	19.56	6.71	0.86	63.27	0.45	3.72	0.88	36.25	2.34	0.80

For the last hybrid, T8SEBCL, the best fitting model results to be Sips model, with an  $R^2$  value of 0.88. The deviation of the  $n_S$  parameter from unity indicates that the material has an heterogeneous surface.

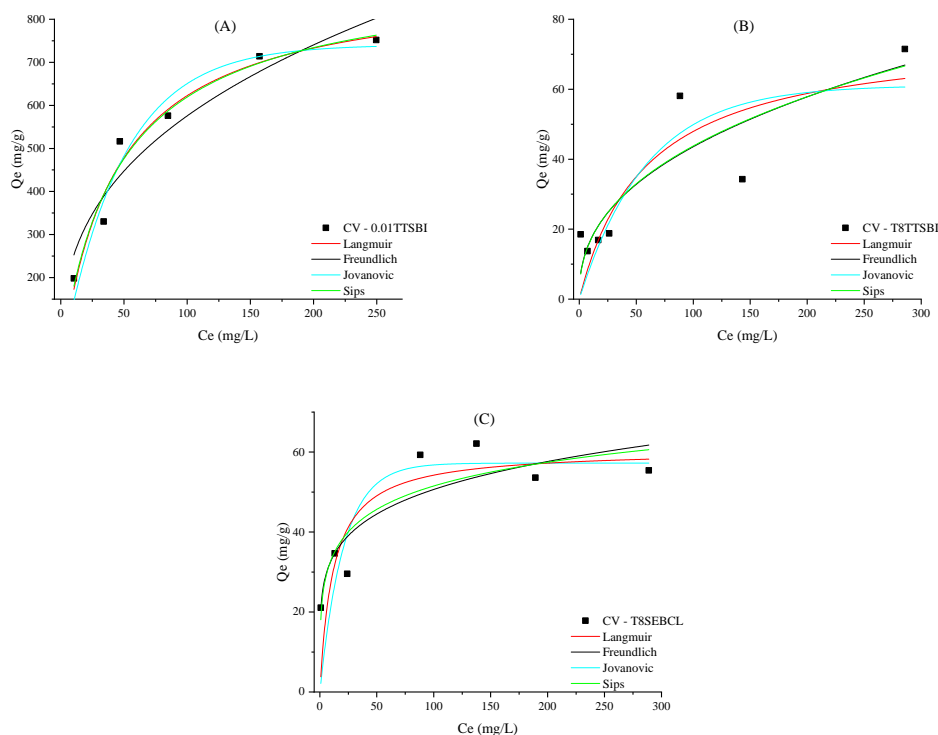


**Figure 5.14.** The Langmuir (red line), Freundlich (black line), Jovanovic (cyan line) and Sips (green line) non-linear isotherm model fitted on initial different concentrations of CV onto 0.01TTSBI (A), T8TTSBI (B) and T8SEBCL (C).

For the adsorption of CV on the 3 hybrids, the isotherms in Figure 5.14 graphically show that the best adsorbent for this dye was 0.01TTSBI, as the adsorption capacity at equilibrium in (A) reaches 700mg/g, compared to (B) and (C) where it reaches 70 and 60 mg/g respectively. The  $R^2$  values show that Sips model is the best fit for all three adsorbents, with  $n_S$  that deviates from 1 for T8TTSBI and T8SEBCL, whereas it is close to 1 for 0.01TTSBI. This can be attributed to the relative size of the dye and the relative expected volume of the pores on the adsorbents. The molecular size of CV, mentioned in Table 4.6, is of  $1.41 \times 1.21 \times 0.65$ nm, therefore it can be reasonable to assume that for 0.01TTSBI the surface results as homogeneous with energetically equivalent sites, which allow the formation of a monolayer. The heterogeneous surface can be explained for T8TTSBI as the expected pore volume is smaller and the structure is less flexible, compared to 0.01TTSBI, while for T8SEBCL the resulting structure is too flexible and apolar, because of the organic saturated hydrocarbon chain, resulting in a poor affinity and scarce interactions. It is also to be noted that the  $R^2$  values for 0.01TTSBI are very close for the Langmuir, Jovanovic and Sips model, indicating that the adsorption process might be a combination of these, which all imply a formation of a monolayer, with eventual interaction between the adsorbing and desorbing molecules.

**Table 5.4.** Summary of Langmuir, Freundlich, Sips and Jovanovic isotherm model parameters for the adsorption of CV on 0.01TTSBI, T8TTSBI and T8SEBCL.

Adsorbent in CV	Langmuir			Freundlich			Sips				Jovanovic		
	$Q_m$ (mg/g)	$K_L$ (L/mg)	$R^2$	$K_F$ (L/g)	$n_F$	$R^2$	$Q_m$ (mg/g)	$K_S$ (L/mg)	$n_S$	$R^2$	$Q_{max}$	$K_J$ (L/mg)	$R^2$
0.01TTSBI	891.16	0.02	0.96	107.96	2.75	0.92	918.79	0.03	1.06	0.97	740.78	0.02	0.96
T8TTSBI	76.00	0.01	0.70	6.63	2.44	0.76	859.43	0.01	2.34	0.76	61.13	0.02	0.67
T8SEBCL	60.60	0.09	0.67	21.44	5.35	0.81	111.32	0.21	3.25	0.82	57.25	0.05	0.65

The same happens between the correlation values of T8TTSBI for Freundlich and Sips model, further indicating that the system is heterogeneous. Furthermore  $n_F > 1$  represents a powerful adsorption. [56]

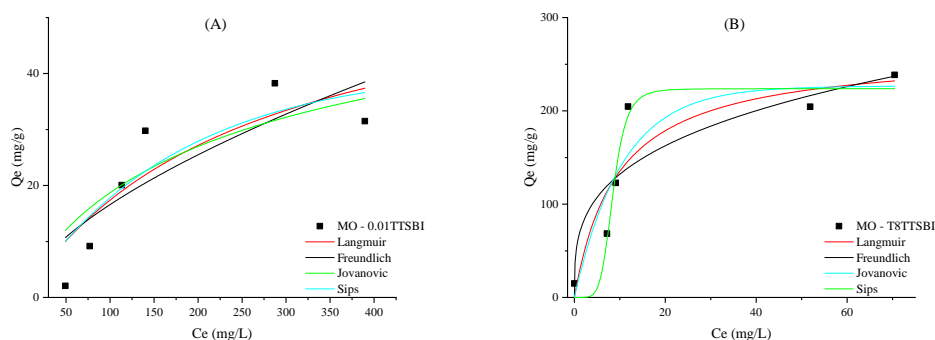


**Figure 5.15.** The Langmuir (red line), Freundlich (black line), Jovanovic (cyan line) and Sips (green line) non-linear isotherm model fitted on initial different concentrations of MO onto 0.01TTSBI (A), T8TTSBI (B) and T8SEBCL (C).

The adsorption of MO was successful only for 0.01TTSBI and T8TTSBI, whereas it resulted in the dissolution of T8SEBCL. The adsorption profiles in Figure 5.15 show a more regular trend for T8TTSBI (B), whereas the curve for 0.01TTSBI (A) seems to have a peak for  $C_e = 287.25$  mg/L and then a decreasing tendency, hence the poor fit given by the adsorption models. The  $R^2$  values for 0.01TTSBI indicate that the best fitting model is Jovanovic model, with a  $Q_{max}$  of 41.14. Instead, the best fitting model for T8TTSBI results to be Sips, with a  $Q_m$  of 223.71. The great difference in adsorption capacity can again be ascribed to the relative size of the dye molecule and the pore size of the adsorbent, as this dye has a molecular size of  $1.31 \times 0.55 \times 0.18$  nm, therefore being the smallest dye molecule used for these tests.

**Table 5.5.** Summary of Langmuir, Freundlich, Sips and Jovanovic isotherm model parameters for the adsorption of MO on 0.01TTSBI, T8TTSBI and T8SEBCL.

Adsorbent in MO	Langmuir			Freundlich			Sips				Jovanovic		
	$Q_m$ (mg/g)	$K_L$ (L/mg)	$R^2$	$K_F$ (L/g)	$n_F$	$R^2$	$Q_m$ (mg/g)	$K_S$ (L/mg)	$n_S$	$R^2$	$Q_{max}$	$K_J$ (L/mg)	$R^2$
0.01TTSBI	61.97	0.004	0.78	0.96	1.61	0.71	62.11	0.01	1.20	0.74	41.14	0.01	0.80
T8TTSBI	263.24	0.11	0.84	66.22	3.33	0.81	223.71	4.4E-6	0.17	0.97	226.59	0.09	0.86

Furthermore, the values of the  $n_S$  parameter for T8TTSBI is of 0.17, which suggests that the process is heterogeneous, hence the surface of the adsorbent presenting energetically different sites.

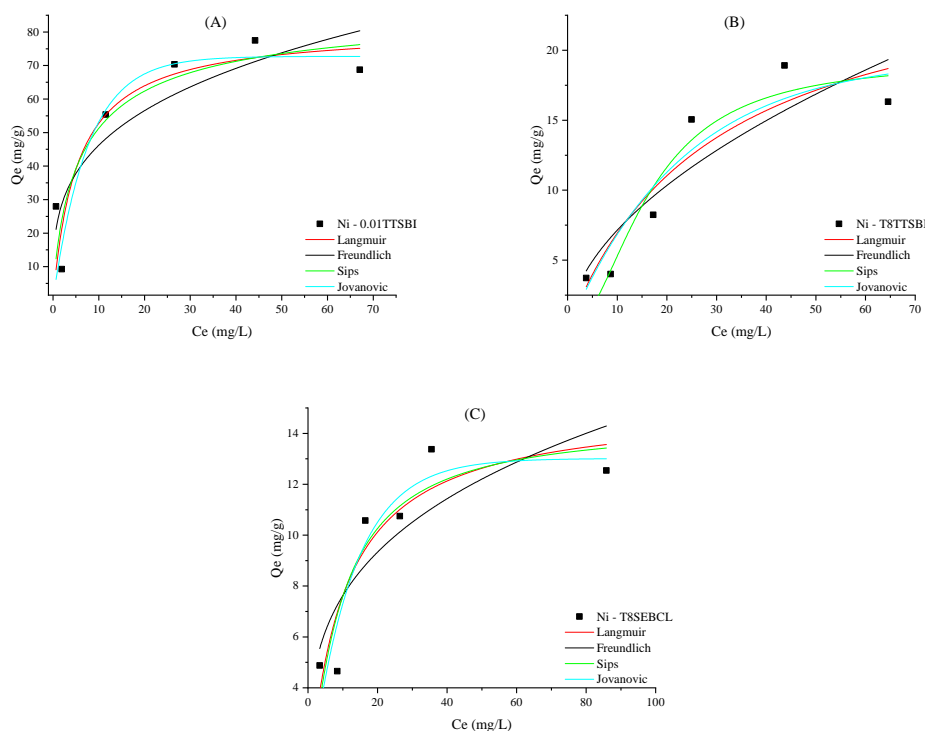


**Figure 5.16.** The Langmuir (red line), Freundlich (black line), Jovanovic (cyan line) and Sips (green line) non-linear isotherm model fitted on initial different concentrations of  $\text{NiCl}_2 \cdot 6\text{H}_2\text{O}$  onto 0.01TTSBI (A), T8TTSBI (B) and T8SEBCL (C).

The profiles for Ni adsorption, reported in Figure 5.16, show the same tendencies seen in the isotherms for the dyes adsorption. The best performing hybrid is 0.01TTSBI, with a  $Q_m$  of 88.38 mg/g, calculated with Sips model. The  $R^2$  for 0.01TTSBI, displayed in Table 5.6, is 0.85 for Sips and Jovanovic models, and the value of  $n_S$  is close to 1, suggesting that the process is homogeneous and that a monolayer is formed. The adsorption isotherm for T8TTSBI, in Figure 5.16 (B), is best predicted by Sips model, with an  $R^2$  of 0.90, followed by Jovanovic model with 0.89. Therefore, the behaviour of T8TTSBI seems to be similar to 0.01TTSBI, in regards to Ni adsorption, however, the  $Q_m$  is only of 19.32 mg/g. This could be due to the T8 structures being vulnerable to pH changes in solution. The  $n_S$  value of 0.50 confirms the tendency shown in dye adsorption for T8TTSBI, further implying the heterogeneity of the surface. Lastly, the best fitting model for T8SEBCL is Jovanovic model, with an  $R^2$  of 0.87, nevertheless, the predicted  $Q_m$  is of 14.6 mg/g from the Sips model, making it, in comparison with T8TTSBI and 0.01TTSBI, the least adsorbent hybrid for Ni. The highly flexible and apolar network can be the cause of such behaviour.

**Table 5.6.** Summary of Langmuir, Freundlich, Sips and Jovanovic isotherm model parameters for the adsorption of  $\text{NiCl}_2 \cdot 6\text{H}_2\text{O}$  on 0.01TTSBI, T8TTSBI and T8SEBCL.

Adsorbent in $\text{NiCl}_2 \cdot 6\text{H}_2\text{O}$	Langmuir			Freundlich			Sips				Jovanovic		
	$Q_m$ (mg/g)	$K_L$ (L/mg)	$R^2$	$K_F$ (L/g)	$n_F$	$R^2$	$Q_m$ (mg/g)	$K_S$ (L/mg)	$n_S$	$R^2$	$Q_{max}$	$K_J$ (L/mg)	$R^2$
0.01TTSBI	81.19	0.19	0.84	23.66	3.44	0.80	88.38	0.22	1.26	0.85	72.74	0.13	0.85
T8TTSBI	27.16	0.03	0.87	2.09	1.87	0.81	19.32	0.004	0.50	0.90	19.50	0.04	0.89
T8SEBCL	15.14	0.10	0.84	3.89	3.41	0.73	14.46	0.08	0.87	0.85	13.01	0.08	0.87

## 5.7 Adsorption kinetics

The kinetic profiles with a fixed concentration of 10mg/L of CV and adsorbent dosage of 10mg are shown in Figure 5.17 for 0.01TTSBI and Figure 5.18 for T8TTSBI.

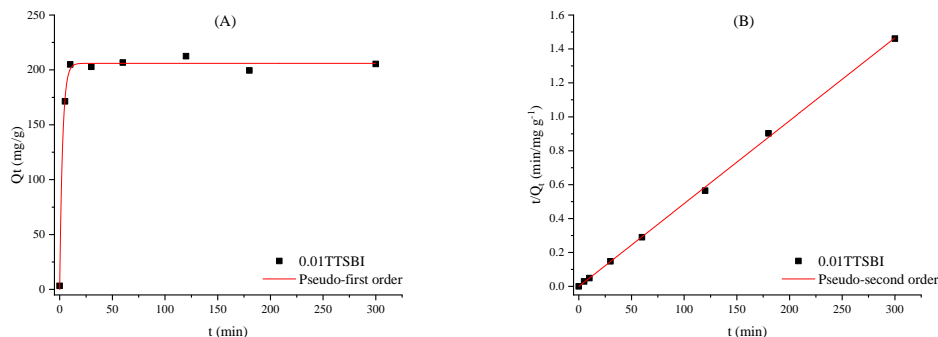


**Figure 5.17.** The pseudo-frist-order (A) and pseudo-second-order (B) kinetic model plots for CV onto 0.01TTSBI.

The removal of CV in 0.01TTSBI is complete in 30 minutes, as the profile, in Figure 5.17 (A) shows an steep increase until 30min and then a plateau. The  $R^2$  values, shown in Table 5.7, result in 0.99 for both the pseudo-first and pseudo-second order models, therefore is reasonable to assume that the kinetic behaviour has characteristics of both models. This means that the adsorption process involves both physisorption and chemisorption, with valency forces through the sharing or exchange of electrons between the adsorbent and adsorbate.

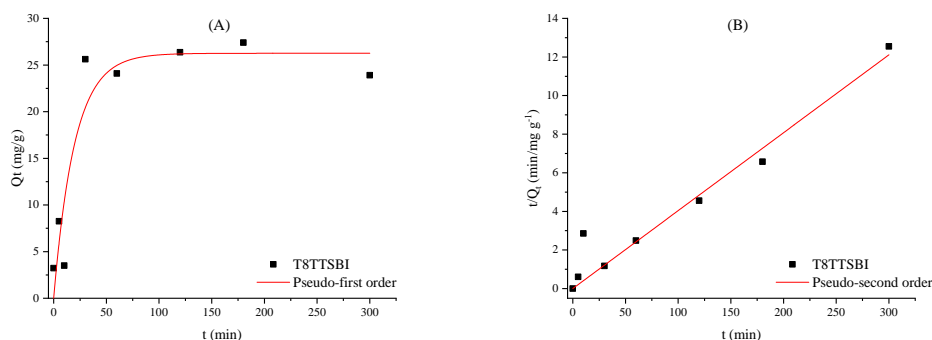


**Figure 5.18.** The pseudo-frist-order (A) and pseudo-second-order (B) kinetic model plots for CV onto T8TTSBI.

The profile for the kinetic behaviour of T8TTSBI, in Figure 5.18 (A), shows that the removal of CV is complete in 60 minutes, however, according to the  $R^2$  values in Table 5.7, the model that has the best prediction for this adsorbent is the pseudo second order, showed in Figure 5.18 (B). This implies that the mechanisms of adsorption is chemisorption.

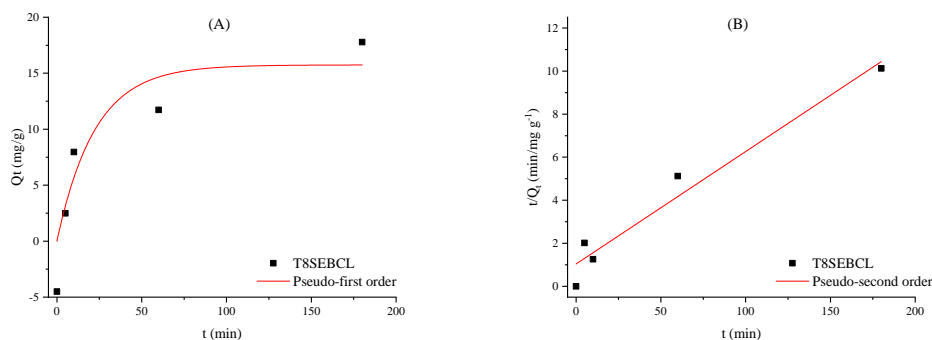


**Figure 5.19.** The pseudo-frist-order (A) and pseudo-second-order (B) kinetic model plots for CV onto T8SEBCL.

The kinetic behaviour of T8SEBCL, shown in Figure 5.19, presents a better fit for the pseudo-second order model, indicating that the mechanism of adsorption is chemisorption. It can be estimated from Figure 5.19 (A) that the adsorbent is saturated after 60 minutes, and the low value for  $k_2$  suggest that a slow adsorption process takes place.

**Table 5.7.** Kinetic parameters for the adsorption of CV on 0.01TTSBI, T8TTSBI and T8SEBCL.

Adsorbent	Pseudo first order			Pseudo second order		
	$Q_{eq}$ (mg/g)	$k_1$ ( $\text{min}^{-1}$ )	$R^2$	$Q_{eq}$ (mg/g)	$k_2$ (g/ mg min)	$R^2$
0.01TTSBI	205.99	0.36	0.99	204.69	5.51	0.99
T8TTSBI	26.26	0.05	0.89	24.77	0.55	0.94
T8SEBCL	15.74	0.04	0.86	19.14	0.003	0.96

When comparing 0.01TTSBI with T8TTSBI, in regards to the adsorption of CV, it appear evident that the first has a greater affinity for this dye, further showed by the values of  $Q_{eq}$  in Tble 5.7, which are of 204.69mg/g for 0.01TTSBI and 24.77mg/g for T8TTSBI. This goes in accordance with the results obtained form the adsorption isotherms in Figure 5.14, and it is ascribed to the relative size of the dye and, given the chemisorption nature of the process, to more favorable interactions between 0.01TTSBI and CV.

## 5.8 Reusability test

A reusability test, described in Section 4.6, was performed on the three hybrids, to evaluate the possibility for regeneration of the materials after adsorption and the for multiple adsorption processes. This test was only successful for 0.01TTSBI, as T8TTSBI and T8SEBACL dissolved in ethanol, during the process of regeneration. This could be due to the fact that once the dye got chemisorbed on the surface of the adsorbents, the consequent affinity of the dye for ethanol caused the solvation of the adsorbent itself.

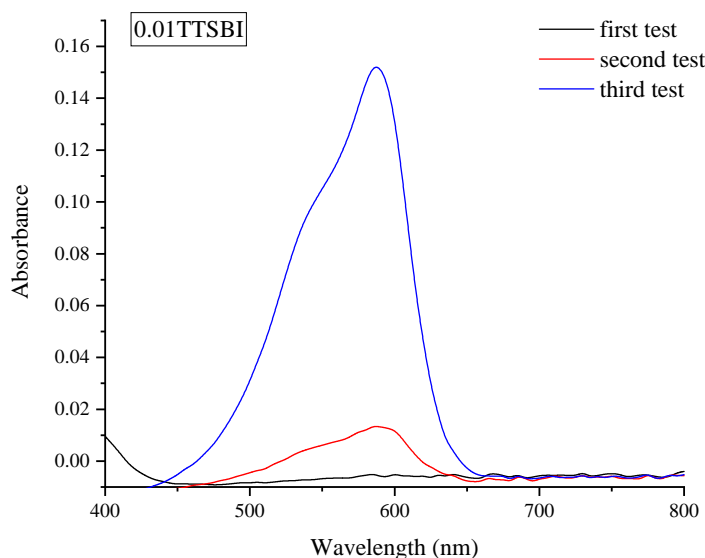


**Figure 5.20.** UV/Vis absorbance spectra for 0.01TTSBI collected after every adsorption/regeneration.

Figure 5.20 shows UV/Vis profiles for 0.01TTSBI with peaks at 590nm, which is the adsorption wavelength for CV. The first test shows almost a nul absorbance, however in the second test, the peak of absorbance reaches 0.01 which corresponds to an equilibrium concentration of 0.50mg/L. In the third test, the equilibrium concentration is of 5.69 mg/L. Considering that the initial concentration of the CV solution was 10 mg/L, the efficiency of removal of 0.01TTSBI decreases quickly.

## 5.9 General discussion

A similar class of hybrids was synthesised in the work of Yang et al. [29] between OVS and ferrocene. The  $Q_m$  obtained in the work are of 66 mg/g and 103mg/g for MO, while in this work the hybrids have a  $Q_m$  of 61.97mg/g for 0.01TTSBI and 263.24 for T8TTSBI, showing, therefore, a better performance. This is not also true for the adsorption capacities regarding MB and CV. The  $Q_m$  obtained in the mentioned article are higher but still comparable to the ones obtained in this work, listed in Tables 5.3and 5.4, as the  $Q_m$  in Yang et al. study are of 417mg/g and 901mg/g for MB and 1440mg/g and 727mg/g for CV. These generally higher values can be the result of more favourable interactions between

ferrocene derivatives, present in their hybrids, and the dye molecules, as ferrocene is also often used as a catalyst. Moreover, DPPF-HPP and DPPOF-HPP present a more rigid framework, when compared to the hybrids synthesised in this work, and their structures present micropores at 1.41 nm and mesopores at 3.79 nm.

**Table 5.8.** Comparison of adsorption capacities of adsorbents for MB.

Adsorbate	Adsorbent	$Q_m$ (mg/g)	Reference
MB	DPPF-HPP	417	[29]
	DPPOF-HPP	277	[29]
	0.01TTSBI	73	This work
	T8TTSBI	97	This work
	T8SEBCL	37	This work

**Table 5.9.** Comparison of adsorption capacities of adsorbents for CV.

Adsorbate	Adsorbent	$Q_m$ (mg/g)	Reference
CV	DPPF-HPP	1440	[29]
	DPPOF-HPP	792	[29]
	0.01TTSBI	891	This work
	T8TTSBI	76	This work
	T8SEBCL	61	This work

**Table 5.10.** Comparison of adsorption capacities of adsorbents for Ni<sup>2+</sup>.

Adsorbate	Adsorbent	$Q_m$ (mg/g)	Reference
Ni <sup>2+</sup>	DPPF-HPP	30	[29]
	DPPOF-HPP	25	[29]
	0.01TTSBI	88	This work
	T8TTSBI	19	This work
	T8SEBCL	14	This work

**Table 5.11.** Comparison of adsorption capacities of adsorbents for MO.

Adsorbate	Adsorbent	$Q_m$ (mg/g)	Reference
MO	DPPF-HPP	66	[29]
	DPPOF-HPP	76	[29]
	0.01TTSBI	62	This work
	T8TTSBI	263	This work

This could suggest that 0.01TTSBI presents greater pore volume and less surface area, as the molecular size of the dyes follows the order CV>MB>MO, and the affinity of 0.01TTSBI for the dyes follows the order CV>MB>MO. Given the small size of MO, the molecule could easily go in and out of pores, while bigger dyes, like CV are trapped into the pores. Additionally, this trend could be also given by favorable electrostatic interaction with the cationic dyes, represented in Figure 5.21, given the electron rich surface of the adsorbent, created by the presence of oxygen and nitrogen atoms. While MO gives repulsive interactions, because of SO<sub>3</sub><sup>-</sup> groups on the dye. However, 0.01TTSBI performs better in regards to Ni<sup>2+</sup>, when compared to the adsorbents in Table 5.10. The expected greater pore volume could facilitate the adsorption of the NiCl<sub>2</sub>\*6H<sub>2</sub>O, while also giving hydrogen bonds with the -OH groups on the surface of the adsorbent.

The adsorption affinity for T8TTSBI is opposite to 0.01TTSBI, as it follows the order of MO>MB>CV. This is true also when comparing T8TTSBI with  $Q_m$  of DPPF-HPP and DPPOF-HPP. This suggest that the organic part plays an important role with regards to the interactions between adsorbent and adsorbate, given that T8TTSBI possesses the same T<sub>8</sub> structure for the inorganic part of the hybrid. However, T8TTSBI presents an electron rich surface, with C=C, C=O, O and N groups, which creates attractive electrostatic interactions with cationic dyes like CV and MB, and repulsive with anionic dyes such as MO. Given that MO is the smallest dye used for testing, it could indicate that the obtained pore volume is fairly small, therefore physically favoring MO, in comparison to CV and MB. The  $Q_m$  for Ni<sup>2+</sup> is of 19 mg/g, in accordance to results from Yang et al. [29], in which the scarce adsorbance for Ni<sup>2+</sup> was related to the small size of the ion, compared to the size of the pores obtained from the silsesquioxane-based hybrids.

The adsorption affinity for T8SEBCL is in the order of CV>MB, which suggests that the network formed is similar in size to 0.01TTSBI. However, the kinetic behaviour indicated

that the principal mechanism of adsorption is chemisorption, therefore, the functional group on the surface play an important role. T8SEBCL presents only =O and N groups on the surface, but is mostly apolar, given the presence of aliphatic carbon chains. This leads to poor electrostatic interactions, and overall, to the least affinity for adsorption of dyes, compared to other adsorbents. The relative better affinity of T8SEBCL for CV could be due to MB small size, which could easily enter end escape the pores of this flexible structure, while CV could be trapped due to its bigger size.

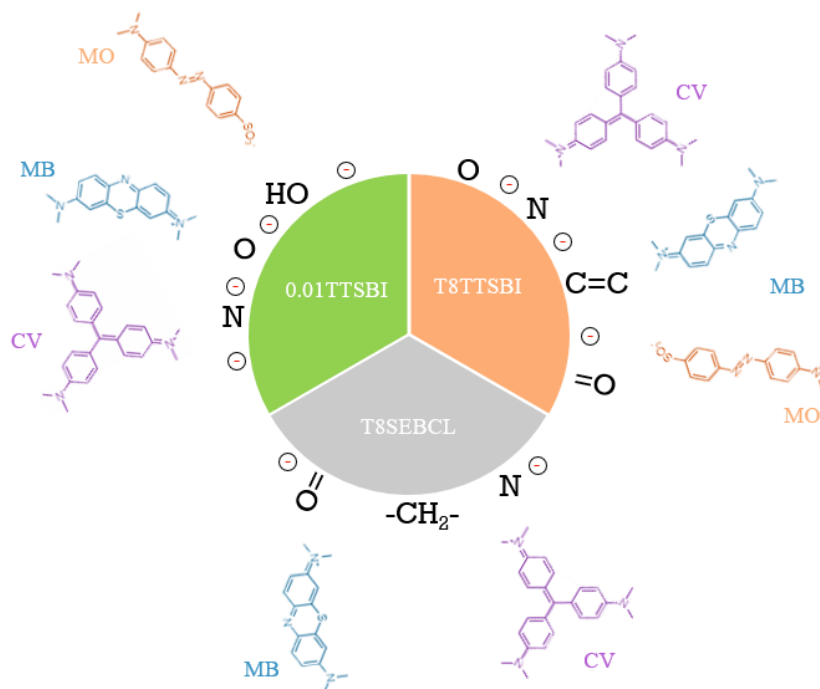


**Figure 5.21.** Schematic representation of surface groups for 0.01TTSBI (green), T8TTSBI (orange) and T8SEBCL (gray), and of dye structures, CV, MB and MO with their functional groups.

The linear form of Langmuir model, displayed in Figure 5.22 (a), (b), (c) and (d), shows more clearly the physical binding of the adsorbate to the adsorbent. The slopes show that 0.01TTSBI is the best, among T8TTSBI and T8SEBCL at adsorbing CV, MB and Ni. While T8TTSBI is the best for MO. This is given by the fact that the slope is calculated as  $1/Q_m$ , hence the lower the slope the higher the affinity. However, Langmuir model is not the best fitting model for T8TTSBI and T8SEBCL, as they resulted to have mostly heterogeneous surfaces and multi-layer formations. The linear Langmuir plots were chosen to display as they can be used to calculate another significant parameter,  $R_L$ . As mentioned in Section 3.4,  $R_L$  is the essential feature of Langmuir model, calculated as in Equation 3.10 and displayed in Figure 5.22 (A), (B), (C) and (D). All the plots show that the values of  $R_L$  fall between 1 and 0, which indicates that the adsorption process is favourable. In addition, lower  $R_L$  values for higher initial concentration of adsorbate indicate that the adsorption was more favorable at higher concentrations. However, the favorability is also related to the irreversibility, given that for  $R_L=0$  the process is irreversible. The linear form of the Langmuir shows good accordance for 0.01TTSBI, confirming the process results in a mono-layer and the distribution of active sites is uniform.

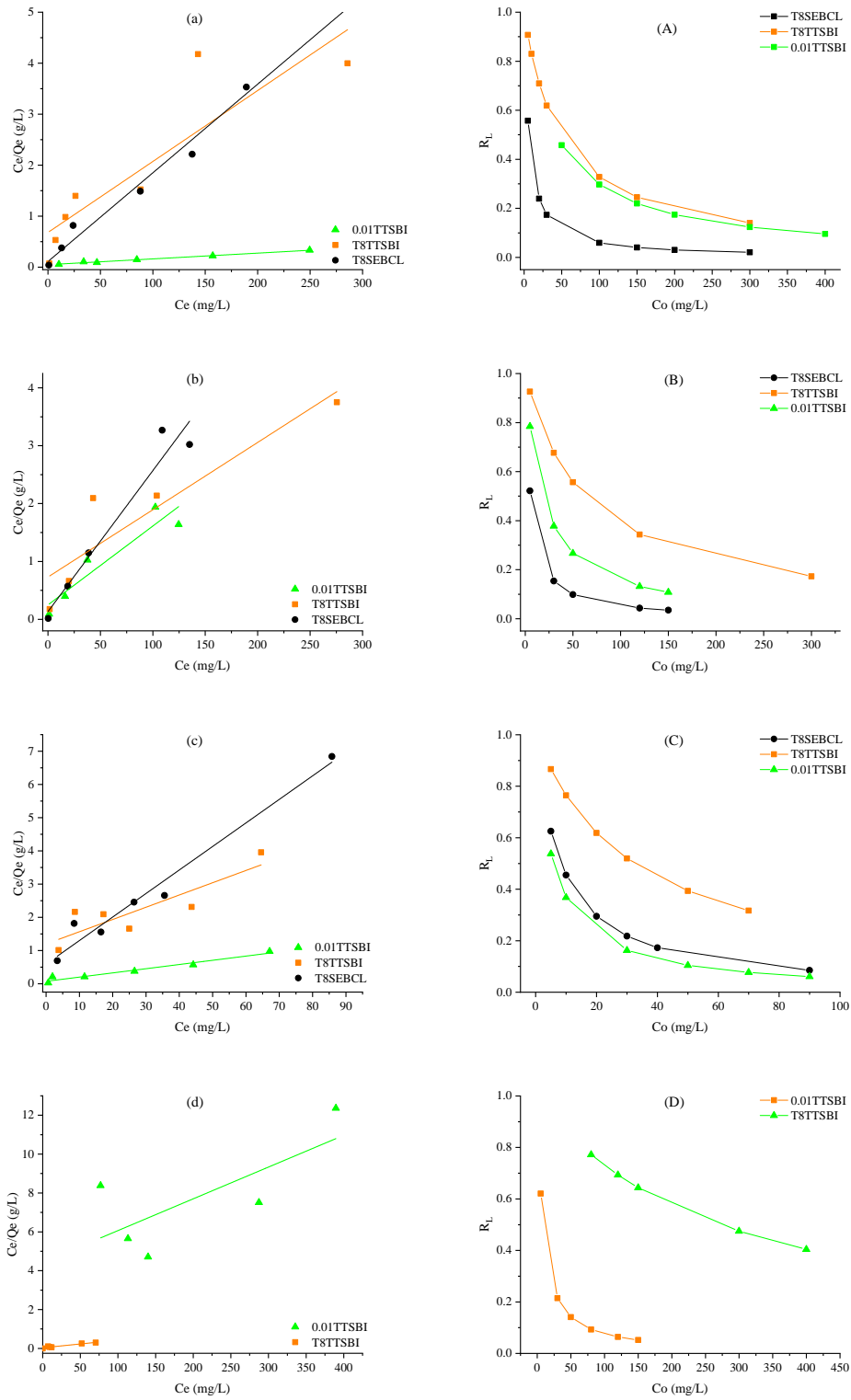


**Figure 5.22.** Langmuir linear plots for CV, MB, Ni and MO, respectively in graph (a), (b), (c) and (d). Plots of  $R_L$  for CV, MB, Ni and MO, respectively in graph (A), (B), (C) and (D).

## 6 Conclusion

In summary, three novel hybrids were successfully synthesised by combining silsesquioxanes and OMIMS. These hybrids proved to have good thermal stability, with their  $T_d$  ranging between 300°C and 400°C. The synthesis are reasonably time consuming, ranging from hours to a day due to their simplicity, even though multi-steps had been involved.

The dye adsorption test gave a strong indication of the difference among the formed structures, as the adsorbent with expected smaller pore size, T8TTSBI, performed better in the adsorption of small dyes, such as MO and MB, and worse for CV. On the other hand 0.01TTSBI, with random SQs structures, and expected greater pore sizes, performed better for CV, which was the biggest dye used for these experiments. The adsorption capacities showed that, all the three hybrids are capable of adsorption, giving  $Q_m$  of 918.79 mg/g, 859.43mg/g and 111.3mg/g for CV in, respectively, 0.01TTSBI, T8TTSBI and T8SEBCL. The great difference of  $Q_m$  between the first two and the last can be ascribed to the less solid network of T8SEBCL. The lack of a solid network proves to be important, as the T8SEBCL hybrid completely dissolves in MO, due to the interactions between the adsorbent and the adsorbate. Therefore, the presence of a strong network is an important characteristic in adsorption processes, and the use of a rigid organic molecule, such as TTSBI, improved the performance of the hybrids. When compared with other porous polymers performances in dye adsorption, these hybrids perform better with small dyes, like MO, instead of larger ones like CV, suggesting the presence of meso- and micropores. Moreover, the adsorbents showed better adsorption capacities when used to adsorb cationic dyes, such as CV and MB, instead of anionic ones such as MO. However, the performance for cationic dye was inferior to hybrids that had P=O as functional groups, suggesting that a more electron rich surface is more favorable. In regards to heavy metal ion adsorption, 0.01TTSBI proved to have high affinity for the adsorption of  $Ni^{2+}$  ions, with a  $Q_m$  of 88 mg/g, while T8TTSBI and T8SEBCL show similar results to literature [29]. Finally, these hybrids resulted to have scarce reusability, as T8TTSBI and T8SEBCL dissolved after the first regeneration, and 0.01TTSBI showed decreasing efficiency after every use.

## 7 Perspective

Waste water treatments are complex process, influenced by many variables. In particular, dyes adsorption processes can be influenced by initial concentration, temperature, pH, adsorption time and adsorbent dosage. The variables explored in this study were the initial concentration and the adsorption time, however, a more in depth study for the effect of pH on the solution could eventually lead to better adsorption capacities, as a it could be a possible reason the solvation of T8SEBCL in MO. Furthermore, temperature dependency studies could give an insight on the overall energy of the system and give further information on the mechanism of adsorption, as to whether it is a chemisorption or an physisorption process. Additionally, different isotherm models could be used to fit the obtained data, as the  $R^2$  values reach, as the highest value, 0.76 for the adsorption of CV on T8TTSBI, suggesting that other models could provide a better prediction for the behaviour of the adsorbent.

For the ease of applicability, this hybrids could also potentially be grafted on membranes for membrane separation processes, as they contain a silica network, which could facilitate the grafting of the hybrid onto silica based membranes. Furthermore, the materials appear to be quite hydrophobic, therefore, potentially increasing the performance of the membrane itself. However, the hydrophobicity should be further investigated with suitable measurements, like contact angle measurements.

Due to time and equipment reasons, a more in depth analysis of the final hybrids was not possible, as the materials present very scarce solubility in usual NMR solvents. Hence, a solid state  $^{29}\text{Si}$  NMR and  $^{13}\text{C}$  NMR could give more information regarding the actual structure of the hybrids, and a gas adsorption study with BET method could reveal the surface area and the actual porosity of the surfaces. Moreover, TGA results coupled with DSC measurements could reveal the formation of different structures, or the formation of a ordered structure for the network, through the observation of the melting peaks.

In this work, the  $\text{T}_8$ -SQs used in the synthesis of the hybrids was the one obtained form HCl catalysis. This was mostly due to practicality and to time constraints, however, with adjustments on the synthesis, especially in regards to solvents and catalyst used during the synthesis of the hybrids, it would be possible to use the  $\text{T}_8$  structures form TFA catalysis.

# Bibliography

- [1] M. Faustini, L. Nicole, E. Ruiz-Hitzky, and C. Sanchez, "History of organic-inorganic hybrid materials: Prehistory, art, science, and advanced applications," *Advanced Functional Materials*, vol. 28, p. 1704158, apr 2018.
- [2] C. Sanchez, H. Arribart, and M. M. G. Guille, "Biomimetism and bioinspiration as tools for the design of innovative materials and systems," *Nature Materials*, vol. 4, pp. 277–288, apr 2005.
- [3] C. Sanchez, B. Julián, P. Belleville, and M. Popall, "Applications of hybrid organic–inorganic nanocomposites," *Journal of Materials Chemistry*, vol. 15, no. 35–36, p. 3559, 2005.
- [4] B. Arkles, "Commercial applications of sol-gel-derived hybrid materials," *MRS Bulletin*, vol. 26, pp. 402–408, may 2001.
- [5] L. Fan, X. Wang, and D. Wu, "Polyhedral oligomeric silsesquioxanes ( POSS )-based hybrid materials: Molecular design, solution self-assembly and biomedical applications," *Chinese Journal of Chemistry*, vol. 39, pp. 757–774, feb 2021.
- [6] M. Soldatov and H. Liu, "Hybrid porous polymers based on cage-like organosiloxanes: synthesis, properties and applications," *Progress in Polymer Science*, vol. 119, p. 101419, aug 2021.
- [7] D. B. Cordes, P. D. Lickiss, and F. Rataboul, "Recent developments in the chemistry of cubic polyhedral oligosilsesquioxanes," *Chemical Reviews*, vol. 110, pp. 2081–2173, apr 2010.
- [8] J.-M. García-Martínez and E. P. Collar, "Organic–inorganic hybrid materials," *Polymers*, vol. 13, p. 86, dec 2020.
- [9] B. M. Novak, "Hybrid nanocomposite materials-between inorganic glasses and organic polymers," *ADVANCED MATERIALS*, vol. 6, pp. 422–433, 1993.
- [10] P. Judeinstein and C. Sanchez, "Hybrid organic–inorganic materials: a land of multidisciplinary," *J. Mater. Chem.*, vol. 6, no. 4, pp. 511–525, 1996.
- [11] Ł. John, "Selected developments and medical applications of organic–inorganic hybrid biomaterials based on functionalized spherosilicates," *Materials Science and Engineering: C*, vol. 88, pp. 172–181, jul 2018.
- [12] C. J. Love, *Synthesis and characterisation of porous polymers*. PhD thesis, University of St Andrews, 2003.
- [13] S. Sulaiman, *Synthesis and Characterization of Polyfunctional Polyhedral Silsesquioxane Cages*. PhD thesis, University of Michigan, 2011.

- [14] Y. Yang, *Synthesis and Rearrangement of Silsesquioxane Cages*. PhD thesis, The Open University Milton Keynes, 2001.
- [15] R. Y. Kannan, H. J. Salacinski, P. E. Butler, and A. M. Seifalian, "Polyhedral oligomeric silsesquioxane nanocomposites: the next generation material for biomedical applications," *Accounts of Chemical Research*, vol. 38, pp. 879–884, aug 2005.
- [16] M. Janeta, Ł. John, J. Ejfler, T. Lis, and S. Szafert, "Multifunctional imine-POSS as uncommon 3d nanobuilding blocks for supramolecular hybrid materials: synthesis, structural characterization, and properties," *Dalton Transactions*, vol. 45, no. 31, pp. 12312–12321, 2016.
- [17] C. Sanchez, F. Ribot, and B. Lebeau, "Molecular design of hybrid organic-inorganic nanocomposites synthesized via sol-gel chemistry," *Journal of Materials Chemistry*, vol. 9, no. 1, pp. 35–44, 1999.
- [18] D. Wang, W. Yang, S. Feng, and H. Liu, "Amine post-functionalized POSS-based porous polymers exhibiting simultaneously enhanced porosity and carbon dioxide adsorption properties," *RSC Advances*, vol. 6, no. 17, pp. 13749–13756, 2016.
- [19] M. Janeta, Ł. John, J. Ejfler, and S. Szafert, "High-yield synthesis of amido-functionalized polyoctahedral oligomeric silsesquioxanes by using acyl chlorides," *Chemistry - A European Journal*, vol. 20, pp. 15966–15974, oct 2014.
- [20] D. Chen, S. Yi, W. Wu, Y. Zhong, J. Liao, C. Huang, and W. Shi, "Synthesis and characterization of novel room temperature vulcanized (RTV) silicone rubbers using vinyl-POSS derivatives as cross linking agents," *Polymer*, vol. 51, pp. 3867–3878, aug 2010.
- [21] A. Lau, *Porous materials : processing and applications*. Burlington: Elsevier Science, 2014.
- [22] D. W. Bruce, D. O'Hare, and R. I. Walton, *Porous Materials*. PAPERBACKSHOP UK IMPORT, Dec. 2010.
- [23] B. S. Ghanem, N. B. McKeown, P. M. Budd, and D. Fritsch, "Polymers of intrinsic microporosity derived from bis(phenazyl) monomers," *Macromolecules*, vol. 41, pp. 1640–1646, feb 2008.
- [24] P. M. Budd, B. S. Ghanem, S. Makhseed, N. B. McKeown, K. J. Msayib, and C. E. Tattershall, "Polymers of intrinsic microporosity (PIMs): robust, solution-processable, organic nanoporous materials," *Chemical Communications*, no. 2, p. 230, 2004.
- [25] D. Wu, F. Xu, B. Sun, R. Fu, H. He, and K. Matyjaszewski, "Design and preparation of porous polymers," *Chemical reviews*, vol. 112, pp. 3959–4015, may 2012.
- [26] H. Zhou, Q. Ye, and J. Xu, "Polyhedral oligomeric silsesquioxane-based hybrid materials and their applications," *Materials Chemistry Frontiers*, vol. 1, no. 2, pp. 212–230, 2017.

- [27] L. Wang and S. Zheng, "Surface morphology and dewettability of self-organized thermosets involving epoxy and POSS-capped poly(ethylene oxide) telechelics," *Journal of Materials Chemistry and Physics*, vol. 136, pp. 744–754, oct 2012.
- [28] V. K. Gupta, P. J. Carrott, M. M. R. Carrott, and Suhas, "Low-cost adsorbents: Growing approach to wastewater treatment—a review," *Critical Reviews in Environmental Science and Technology*, vol. 39, pp. 783–842, oct 2009.
- [29] X. Yang and H. Liu, "Diphenylphosphine-substituted ferrocene/silsesquioxane-based hybrid porous polymers as highly efficient adsorbents for water treatment," *ACS Applied Materials & Interfaces*, vol. 11, pp. 26474–26482, jul 2019.
- [30] V. Katheresan, J. Kansedo, and S. Y. Lau, "Efficiency of various recent wastewater dye removal methods: A review," *Journal of Environmental Chemical Engineering*, vol. 6, pp. 4676–4697, aug 2018.
- [31] S. D. Gisi, G. Lofrano, M. Grassi, and M. Notarnicola, "Characteristics and adsorption capacities of low-cost sorbents for wastewater treatment: A review," *Sustainable Materials and Technologies*, vol. 9, pp. 10–40, sep 2016.
- [32] C. Erkey and M. Türk, "Thermodynamics and kinetics of adsorption of metal complexes on surfaces from supercritical solutions," in *Synthesis of Nanostructured Materials in Near and/or Supercritical Fluids - Methods, Fundamentals and Modeling*, pp. 73–127, Elsevier, 2021.
- [33] X. Yang and H. Liu, "Ferrocene-functionalized silsesquioxane-based porous polymer for efficient removal of dyes and heavy metal ions," *Chemistry - A European Journal*, vol. 24, pp. 13504–13511, aug 2018.
- [34] N. B. McKeown, "Organic molecules of intrinsic microporosity," *Organic Materials*, vol. 02, pp. 020–025, jan 2020.
- [35] A. E. Danks, S. R. Hall, and Z. Schnepf, "The evolution of 'sol-gel' chemistry as a technique for materials synthesis," *Materials Horizons*, vol. 3, no. 2, pp. 91–112, 2016.
- [36] C. Brinker, *Sol-gel science : the physics and chemistry of sol-gel processing*. Boston: Academic Press, 1990.
- [37] S. Esposito, "“traditional” sol-gel chemistry as a powerful tool for the preparation of supported metal and metal oxide catalysts," *Materials*, vol. 12, p. 668, feb 2019.
- [38] I. Strawbridge, A. Craievich, and P. James, "The effect of the h<sub>2</sub>o/TEOS ratio on the structure of gels derived by the acid catalysed hydrolysis of tetraethoxysilane," *Journal of Non-Crystalline Solids*, vol. 72, pp. 139–157, jun 1985.
- [39] B. E. Yoldas, "Monolithic glass formation by chemical polymerization," *Journal of Materials Science*, vol. 14, pp. 1843–1849, aug 1979.
- [40] S. Torquato, "Perspective: Basic understanding of condensed phases of matter via packing models," *The Journal of Chemical Physics*, vol. 149, p. 020901, jul 2018.

- [41] N. B. McKeown and P. M. Budd, "Polymers of intrinsic microporosity (PIMs): organic materials for membrane separations, heterogeneous catalysis and hydrogen storage," *Chemical Society Reviews*, vol. 35, no. 8, p. 675, 2006.
- [42] P. Bruice, *Organic chemistry*. Upper Saddle River, NJ: Pearson/Prentice Hall, 2004.
- [43] J. Peyrton and L. Avérous, "Aza-michael reaction as a greener, safer, and more sustainable approach to biobased polyurethane thermosets," *ACS Sustainable Chemistry & Engineering*, vol. 9, pp. 4872–4884, mar 2021.
- [44] M. Magosso, M. van den Berg, and J. van der Schaaf, "Kinetic study and modeling of the schotten–baumann synthesis of peroxyesters using phase-transfer catalysts in a capillary microreactor," *Reaction Chemistry & Engineering*, vol. 6, no. 9, pp. 1574–1590, 2021.
- [45] N. Ayawei, A. N. Ebelegi, and D. Wankasi, "Modelling and interpretation of adsorption isotherms," *Journal of Chemistry*, vol. 2017, pp. 1–11, 2017.
- [46] S. Mustapha, D. T. Shuaib, M. M. Ndamitso, M. B. Etsuyankpa, A. Sumaila, U. M. Mohammed, and M. B. Nasirudeen, "Adsorption isotherm, kinetic and thermodynamic studies for the removal of pb(II), cd(II), zn(II) and cu(II) ions from aqueous solutions using albizia lebbeck pods," *Applied Water Science*, vol. 9, jul 2019.
- [47] Y. HO, "Review of second-order models for adsorption systems," *Journal of Hazardous Materials*, vol. 136, pp. 681–689, aug 2006.
- [48] Y. Kaneko, M. Shoiriki, and T. Mizumo, "Preparation of cage-like octa(3-aminopropyl)silsesquioxane trifluoromethanesulfonate in higher yield with a shorter reaction time," *Journal of Materials Chemistry*, vol. 22, no. 29, p. 14475, 2012.
- [49] Y. Lu, W. Wang, X. Jin, G. Xiao, Z. Hu, and T. Wang, "Synthesis and gas separation properties of intrinsic microporosity polymer pim-1," in *Proceedings of the 5th International Conference on Advanced Design and Manufacturing Engineering*, pp. 94–98, Atlantis Press, 2015/10.
- [50] D. Magdziak, A. A. Rodriguez, R. W. V. D. Water, and T. R. R. Pettus, "Regioselective oxidation of phenols to o-quinones with o-iodoxybenzoic acid (IBX)," *Organic Letters*, vol. 4, pp. 285–288, jan 2002.
- [51] N. Saadatkah, A. C. Garcia, S. Ackermann, P. Leclerc, M. Latifi, S. Samih, G. S. Patience, and J. Chaouki, "Experimental methods in chemical engineering: Thermogravimetric analysis—TGA," *The Canadian Journal of Chemical Engineering*, vol. 98, pp. 34–43, dec 2019.
- [52] M. Belhachemi and F. Addoun, "Comparative adsorption isotherms and modeling of methylene blue onto activated carbons," *Applied Water Science*, vol. 1, pp. 111–117, sep 2011.
- [53] teresa OH and C. K. Choi, "Comparison between SiOC thin film by plasma enhance chemical vapor deposition and SiO<sub>2</sub> thin film by fourier transform infrared spectroscopy," *Journal of the Korean Physical Society*, vol. 56, pp. 1150–1155, apr 2010.

- [54] N. Aktaş, N. Şahiner, Ömer Kantoğlu, B. Salih, and A. Tanyolaç, “Biosynthesis and characterization of laccase catalyzed poly(catechol),” *Journal of Polymers and the Environment*, vol. 11, no. 3, pp. 123–128, 2003.
- [55] R. Ranjan and W. J. Brittain, “Combination of living radical polymerization and click chemistry for surface modification,” *Macromolecules*, vol. 40, pp. 6217–6223, jul 2007.
- [56] H. Shahbeik, N. Bagheri, S. Ghorbanian, A. Hallajisani, and S. Pourkarimi, “A new adsorption isotherm model of aqueous solutions on granular activated carbon,” *World Journal of Modelling and Simulation*, vol. 9, pp. 243–254, 11 2013.
- [57] E. D. von Meerwall, *Spectroscopy: NMR, Fluorescence, FT-IR*. Springer-Verlag Verlag Berlin Heidelberg, 1984.
- [58] T. Hasegawa, *Quantitative Infrared Spectroscopy for Understanding of a Condensed Matter*. Springer, 2017.
- [59] D. C. Harris, *QUANTITATIVE CHEMICAL ANALYSIS*. Clancy Marshall, 2010.

# A Analysis Methods

This section will serve as an overview of the analysis methods used for this project, in which the base principals and the type of information obtained from each analysis will be described.

## A.1 Attenuated total reflection FT-IR

The analysis method FT-IR in adsorption measures molecular vibrations induced by the infra-red region of the electromagnetic spectrum. It is therefore used to asses the presence of certain functional groups or obtain some information regarding the molecular structure. FT-IR is generally done on liquid samples, but for solid samples a more suitable method is Attenuated Total reflection FT-IR (ATR FT-IT). This analysis measures the changes that occur in a totally internally reflected infrared beam when the beam comes into contact with the sample, which is placed directly on the surface of an internal reflection plate or prism. Virtually, the IR radiation reaches the plate or the prism where the sample is placed, so that when the sample shows absorption the penetrating wave is reflected and attenuated, so that the reflectance can be measured as in Equation A.1

$$R = I - kd_c \tag{A.1}$$

Where R is the reflectance, k is the absorption coefficient, I is the energy of the incident wave and  $d_c$  is the effective layer thickness. The ATR is the resulting energy loss in the reflected wave. Therefore, this technique is preferred when measuring the spectra of a strongly absorbing thick sample, because it reduces the absorbance. [57, 58]

## A.2 Nuclear magnetic resonance

Nuclear magnetic resonance (NMR) is used to identify the framework of an organic compound, and it is a spectroscopy in adsorption based on resonance. All atomic particles posses an intrinsic angular momentum of spin (P), therefore, spinning charged particles generate a magnetic field, giving the atom a dipolar magnetic momentum ( $\mu$ ). If the nuclei posses an even number of protons and neutrons, the spin will even out, giving a total 0 spin for the atom. Whereas, when the the sum of protons and neutrons in the atom is uneven, the nuclei will have a  $\mu$ , which depends on the quantized P according to Equation A.2

$$P = \sqrt{I(I + 1)} \frac{h}{2\pi} \tag{A.2}$$

Where h is Bohr's constant and I is the quantic number of nuclear spin, which will have +1/2 and -1/2 values for atoms with an uneven number of protons and neutrons. Therefore, when the nuclei gets exposed to an external magnetic field (B), the spins will align with or against it, generating, respectively, protons in a lower energy  $\alpha$ -spin state, and protons in

a higher energy  $\beta$ -spin state. The energy difference ( $\Delta E$ ) between the two states depends on the strength of the applied B according to Equation A.3

$$\Delta E = \frac{\gamma h B}{2\pi} = h\nu \quad (\text{A.3})$$

where  $\nu$  is the frequency of the applied radiation and  $\gamma$  is the gyromagnetic ratio, which depends on the particular kind of nucleus. The difference in the signal of a particular nucleus read on the spectrum will be given by the effect of "shielding". This effect is caused by nearby electron clouds, which will decrease or increase the effective magnetic field perceived by each nucleus, thus the nuclei near dense electron clouds will be more shielded and present a signal at low frequencies. The opposite will happen for deshielded nuclei. The position at which a signal occurs is called the chemical shift ( $\delta$ ). [42]

### A.3 Thermogravimetric analysis

The group of techniques which concern monitoring changes of physical or chemical properties of a sample with time as it is subjected to a temperature program are called thermal analysis (TA). When the measurements record also the mass, time and temperature, the technique is called thermogravimetric analysis (TGA). [51] TGA is quantitative analytical technique, which gives information regarding kinetics and mechanisms for any process that involves a change in mass by isothermal, non-isothermal, and quasi-isothermal methods. Moreover, it can give information regarding material thermal stability, oxidative stability, multicomponent composition, product lifetime, decomposition kinetics, and moisture and volatile content. The weight of the sample is taken by a precise micro balance, inside the apparatus, which is connected to the sample pan inside the furnace. The mass of the sample decreases as temperature increases, as the material decomposes and the volatile compounds evaporate or the oxidation state decreases. Besides the temperature program, other variables can be controlled, for instance the gaseous environment, which can be inert, redox or simply reactive. When this technique is coupled with differential scanning calorimetry (DSC), it can characterize transitions like melting, crystallisation, glass transition, and solid-solid transition, helping to deconvolute the DSC plot by separating physical changes from chemical changes.

The resulting data is plotted in a thermogram, which usually represents the change in mass vs temperature or time, and each material has a unique curve. These graphs have multiple sections, delimited by temperature ranges in which certain physical changes usually happen. Below 150° all the physisorbed water, solvents, trapped gases and volatile compounds leave the sample. Between 150°C and 250°C all the chemisorbed species leave the sample. Above 250°C, the compounds in the material start to decompose, giving an onset and endset temperature for each component of the material. Besides the endset, and eventual mass increase could be seen if the environment is oxidising.

### A.4 Ultra violet and visible spectroscopy

Ultra violet and visible (UV/Vis) spectroscopy employs electromagnetic radiation with wavelengths ( $\lambda$ ) ranging between 200 and 800 nm to provide information about compounds with conjugated double bonds. This is possible due to UV/Vis light having the right energy

to cause a transition of an electron between two orbitals, as wavelengths are inversely related to energy by the following Equation A.4

$$E = \frac{hc}{\lambda} \quad (\text{A.4})$$

Where  $E$  is the energy,  $h$  is Planck's constant, and  $c$  is speed of light. Therefore, the shorter the wavelength, the greater the energy produced by the radiation. When a molecule is hit by a radiation of appropriate wavelength it absorbs the radiation and an electron is promoted from its ground state to an excited state, and this is called an electronic transition. UV/Vis light is powerful enough to promote non bonding electron ( $n$ ) into a antibonding molecular orbital ( $\pi^*$ ), or an electron from a bonding ( $\pi$ ) to a ( $\pi^*$ ). These transitions can also be written as  $n \rightarrow \pi^*$  and  $\pi \rightarrow \pi^*$ . [42] Each molecule has a characteristic  $\lambda_{max}$ , which is the wavelength corresponding to the maximum absorbance of the absorption band. This type of analysis is also relevant to determine the concentration of various compounds, as the relation between absorbance ( $A$ ) and concentration is given by the Lambert-Beer law A.5

$$A = cl\epsilon \quad (\text{A.5})$$

where  $c$  is the concentration of the sample,  $l$  is the length of the light path thorough the sample and  $\epsilon$  is the molar absorptivity, which is constant and characteristic of each compound. Therefore, when the compound is known, it becomes very simple to build a standard curve and determine the concentration of samples of unknown concentration. [42]

## A.5 Atomic absorption spectroscopy

Atomic absorption spectroscopy (AAS) is a type of analysis similar to UV/Vis spectroscopy, as it provides information about the presence and concentration of certain analytes, when the sample is irradiated with an radiation of appropriate wavelength. However, a significant difference between the two methods lies in the fact that the width of absorption or emission bands of gaseous atoms consist of sharp lines with widths of 0.001 nm, compared to the bandwidths of 10 to 100 nm typically obtained from molecular spectroscopy.

in AAS a liquid sample is first aspirated into a flame, whose temperatures can vary between 2000-3000°K, depending on the gas burned to create the flame. Here all the liquids evaporate and the solids get atomized. The length of the flame becomes the path length in the Lambert-Beer equation, and is typically 10cm. The radiation that excites the sample is generated by an hollow-cathode lamp, in which the cathode is typically made of the same analyte in analysis. When the cathode is bombarded with energetic  $\text{Ne}^+$  or  $\text{Ar}^+$  ions, excited atoms vaporize from the surface and emit light with the same frequencies absorbed by analyte in the flame. On the other side of the flame a detector measures the amount of light that passes through the flame. [59]